Engineering Geology 294 (2021) 106384

Contents lists available at ScienceDirect

Engineering Geology

journal homepage: www.elsevier.com/locate/enggeo

Triggers and consequences of landslide-induced impulse waves – 3D dynamic reconstruction of the Taan Fiord 2015 tsunami event

Andrea Franco[a,*], Jasper Moernaut[b], Barbara Schneider-Muntau[c], Michael Strasser[b], Bernhard Gems[a]

[a] Unit of Hydraulic Engineering, University of Innsbruck, Technikerstraße 13, 6020 Innsbruck, Austria
[b] Institute of Geology, University of Innsbruck, Innrain 52f, 6020 Innsbruck, Austria
[c] Unit of Geotechnical and Tunnel Engineering, University of Innsbruck, Technikerstraße 13, 6020 Innsbruck, Austria

ARTICLE INFO

Keywords:
Landslide-induced impulse wave
Multi-hazards
Wave dynamics
Granular media
Flow3D

ABSTRACT

Natural multi-hazards as landslide-induced tsunamis require a multi-disciplinary approach to analyze the cascade effects that pose a significant threat to mountain communities and the surrounding territory. This paper comprises a detailed study of both the landslide evolution and the wave dynamics of the October 2015 Taan Fiord (Alaska) tsunami event, which represents a highly valuable case study for generic methodology development of single code applications using the numerical software Flow3D and testing its applicability for cascading wave hazard evaluation. First, a geomorphological analysis of the unstable slope is performed by elaborating diverse digital elevation models, where a significant vertical displacement of −90 m is observed before the final collapse, and the influence of listric faults within the slide body results in a bulging of the glacier at the toe. Data from time-series analyses suggests that the glacier retreat (and the reduction of local buttresses) critically destabilized the slope leading to the October 2015 catastrophic failure. The reconstructed landslide volume is estimated to be 49.4 Mm^3, where 26 Mm^3 entered the fiord and triggered the tsunami. Second, wave dynamics are recreated with Flow3D. Both dense fluid and granular media models are used and compared to verify their performance in initiating the impulse wave, where a measured impact speed ranging between 32 and 49 ms^{-1} triggers a maximum wave amplitude of about 95–99 m. the maximum run-up of 193 m at the Hoof Hill Fan is recreated with both approaches, but general overestimations (about 9–12%) compared to the observations, in the impact area, are computed for the inundation process. A good approximation of the observed run-up along the entire length of the fiord is found for wave propagation models using the granular media approach. Beyond the Taan-Fiord case study and for evaluation of cascading landslide-induced hydraulic hazard in other settings, this work points out (i) the necessity of using a high temporal resolution of digital elevation models to analyze the multi-stage slope failure and to properly estimate the landslide volume, (ii) the applicability of the applied numerical models to reproduce the wave dynamics of a landslide-induced tsunami event on one code only, and (iii) how these models can be adopted to develop hazard maps related to potential wave hazards in natural basins.

1. Introduction

1.1. Natural hazards as consequences of ongoing climate change

The concept of natural multi-hazards in mountain regions recently emerged in the scientific community due to the increasing awareness of potential chain reactions between different phenomena, with potentially devastating effects on the human environment (Duc et al., 2020). Climate change leads to an increase in intensities and occurrences of natural hazards (Higman et al., 2018; Haque et al., 2019; Mergili et al., 2020; Nie et al., 2021), thus increasing the exposure to danger in critical areas. Landslides, rockslides or large mass movements are often linked to the retreat of glaciers in high mountain regions (such as the Alps and the Andes) or fiords found on Arctic coasts. Climate change is causing glaciers to disappear (Koppes and Hallet, 2006; Williams and Koppes, 2019; Dai et al., 2020), which can reveal fragile slopes upon water

* Corresponding author.
E-mail address: andrea.franco@uibk.ac.at (A. Franco).

https://doi.org/10.1016/j.enggeo.2021.106384
Received 21 January 2021; Received in revised form 9 September 2021; Accepted 16 September 2021
Available online 24 September 2021

bodies (Roe et al., 2017; Higman et al., 2018). Previous glacier compressions on the rock caused stress fractures (Deline et al., 2015), and the consequent lack of stabilizing glacial ice on steep slopes, coupled with the thawing of permafrost, increases the possibility of slopes failure and collapse with catastrophic effects (Gruber and Haeberli, 2007; Deline et al., 2015; Kos et al., 2016; Coe et al., 2018). Another consequence of glacial retreat is the formation or extension of deep-water bodies, such as mountain lakes or fiords in glacially eroded basins bordered by steep and potentially unstable slopes (Haritashya et al., 2018; Harrison et al., 2018). All the mentioned conditions may precondition and trigger natural hazards such as landslide-induced impulse waves in mountain water basins. Settlements and touristic attractions have been, and keep being built near Alpine lakes or Arctic fiords, increasing the need to analyze natural hazards considering cascade effects.

Several landslide-induced tsunami (L.I.T.) events have occurred over the last century (see compilation in Franco et al., 2020). Numerous studies have contributed to gaining a better understanding of these phenomena by analyzing past events and adopting different methods, like physical scale experiments (Fritz et al., 2001; Bregoli, 2015; Romano et al., 2016; Kim et al., 2020) and derived analytical equations (Walder et al., 2003; Heller, 2009; Heller and Hager, 2010) or numerical models (Das et al., 2009; Pastor et al., 2009; Basu et al., 2009; Gabl et al., 2015; Sassa et al., 2016; Zhao et al., 2016; Mao et al., 2017; Ersoy et al., 2019; Kafle et al., 2019; Bilal et al., 2021) to reproduce the landslide-generated tsunami and its downstream effects (Ward and Day, 2010; Gauthier et al., 2018; Gonzalez-Vida et al., 2019; Paris et al., 2019; Du et al., 2020; Wang et al., 2015, 2019, 2021; Franco et al., 2020; Franci et al., 2020, 1; Karahan et al., 2020).

The main goal of ongoing research is to develop tools for forecasting L.I.Ts. and to guide appropriate mitigation measures to prevent such disasters. With the increase in computational power over the last decades, numerical modeling approaches are commonly used to simulate a L.I.T. event. Modeling a landslide-tsunami requires recreating the different stages of the entire complex phenomena, which includes i) the landslide process, ii) the interaction between the slide and the water body (or wave initiation), and iii) wave propagation and iv) inland inundation. Different methodologies such as the Non-linear Shallow Water Equations, the Boussinesq method, and the Reynolds-Averaged-Navier-Stokes Equations (RANS) have been applied to better recreate wave dynamics out of an impact process (Zhang et al., 2020). Since the majority of the existing single-codes for landslide-tsunami simulation are based on wave propagation theory, where Newtonian or non-Newtonian fluids are used to recreate the sliding process, the interaction between the solid slide material and water is not considered. Indeed, to model properly the different processes, separate decoupled numerical codes might be needed (Wang et al., 2019). An example is provided by Tan et al. (2018) who adopt two distinct models, Dual-SPHysics (an advanced Smoothed Particle Hydrodynamics method) for the impact and tsunami initiation, and SWASH for the further wave propagation. The first approach is appropriate for the generation process but has some limitations in reproducing a physical wave decay at long distances. Contrarily, the second appears to be reliable in recreating the wave propagation. The use of decoupled codes has been recently solved through the integration and development of innovative single codes that model both landslide motion and wave dynamics by defining appropriate landslide rheology and applying wave equations such as r.avaflow (Pudasaini and Mergili, 2019), the coupled SPH-DEM based code (Xu et al., 2020), or Splash3D (Wu et al., 2020). Other codes account for the momentum transfer with the implementation of the "Push Ahead" and "Drag Along" accelerations such as in the "Tsunami Square Approach" (Wang et al., 2021). Nonetheless, a limiting factor for the numerical model set-up is often linked to the data availability (due to a lack of observations and detailed field investigations) which is relevant for the definition of the input parameters and boundary conditions (like the topographic or bathymetric surface). The large request of specific input data can be obviated by the use of simplified and less-data demanding codes which are still suitable in reproducing a L.I.T. event (in eg. Flow3D, Alvarez and Wendelbo, 2018).

As one of the best-documented cases (Higman et al., 2018), the recent tsunami event in Taan Fiord (Icy Bay, Alaska, Fig. 1) in October 2015 represents a good opportunity to analyze the whole process chain (landslide and wave dynamics) in detail from a multidisciplinary perspective, given a large amount of new information and data. Indeed, this work aims to reproduce the Taan Fiord tsunami event while testing specific and complex modeling approaches for wave initiation. Additionally, an in-depth analysis of wave dynamics in both near (at the terminus of the Tyndall Glacier) and in the far-field (towards the mouth of the fiord) is provided.

Initially, geomorphological analysis based on an elaboration of DEMs is carried out, requiring the availability of new data (Arctic DEM AK·V2–2014), to better understand the landslide evolution and to estimate the total remobilized. The computational fluid dynamics (CFD) software Flow3D v.12.2 is applied to model the L.I.T. at the Taan Fiord. A fluid-like volume sliding down the slope represents the trigger for tsunami generation and propagation. Once the wave dynamics and the run-up are well recreated in the impact area, the wave propagation is modeled to reproduce the inundation along the full fiord length (about 17 km from the slide source to the mouth).

Given the range of available input data, for each described process, a discussion on the changes in outputs for different inputs is proposed. A final discussion provides insights regarding the advantages and limitations of using the different modeling approaches to generate an impulse wave in a natural water basin and the analysis of the implications for wave hazard assessment. Additionally, hazard maps are presented as a valuable tool to generally assess flood risk concerning L.I.T. in mountain water basins.

1.2. The Taan Fiord and the 2015 tsunami event

The Taan Fiord, a branch of the Icy Bay, is located on the south coast of Alaska (part of the Wrangell St. Elias National Park), with a length of about 17 km. Today the fiord is divided into two basins, one in the north (maximum depth about 100 m) and one in the south-west (depth of 130 m), separated by a ridge in the middle with a shallower depth of about 50 m (Fig. 1). The width varies from 1.0–1.5 km in the north and 2.0–4.5 km in the southwest; the mouth of the fiord has a width of about 2.7 km. The Icy Bay is located in a tectonically active area (Higman et al., 2018) due to the ongoing collision between the North American plate and the Yakutat microplate (Pavlis et al., 2012). The Taan Fiord lays in the hanging wall of the Malaspina thrust fault. From 1991, the Tyndall glacier terminus remains along the Chaix Hills thrust fault (*E*-W oriented, Dufresne et al., 2018; Haeussler et al., 2018), which accommodates the rapid tectonic uplift (about 4–5 mma^{-1}) of weak lithified rock from the Miocene-Holocene to elevations high in the St. Elias mountains system (Meigs et al., 2006). Significant seismo-tectonic activity, as illustrated by several large-magnitude historical earthquakes (Dufresne et al., 2018), further increases the potential of catastrophic rock slope failures in this region (Haeussler et al., 2018). At the Taan Fiord, the steep slopes, mostly made of weakly lithified sedimentary rock, surround the fiord rising to 900 m a.s.l (Williams and Koppes, 2019). Significant environmental changes occurred in the last century resulting from rapid glacier retreat which exposed a large part of these rock slopes. New fan deltas formed at the fiord coastline between 1961 and 1991 (Bloom et al., 2020) as results of new fluvial tributaries from the retreating glaciers (eg. the Hoof Hill Fan at the head of the fiord, Fig. 1).

The recent L.I.T. event at the Taan Fiord on 17th October 2015 represents a catastrophic response to these important geomorphological-climate changes at Icy Bay. On this date, a landslide impacted the fiord (and partially the glacier at the head of the fiord), triggering an impulse wave with an estimated maximum wave crest (or

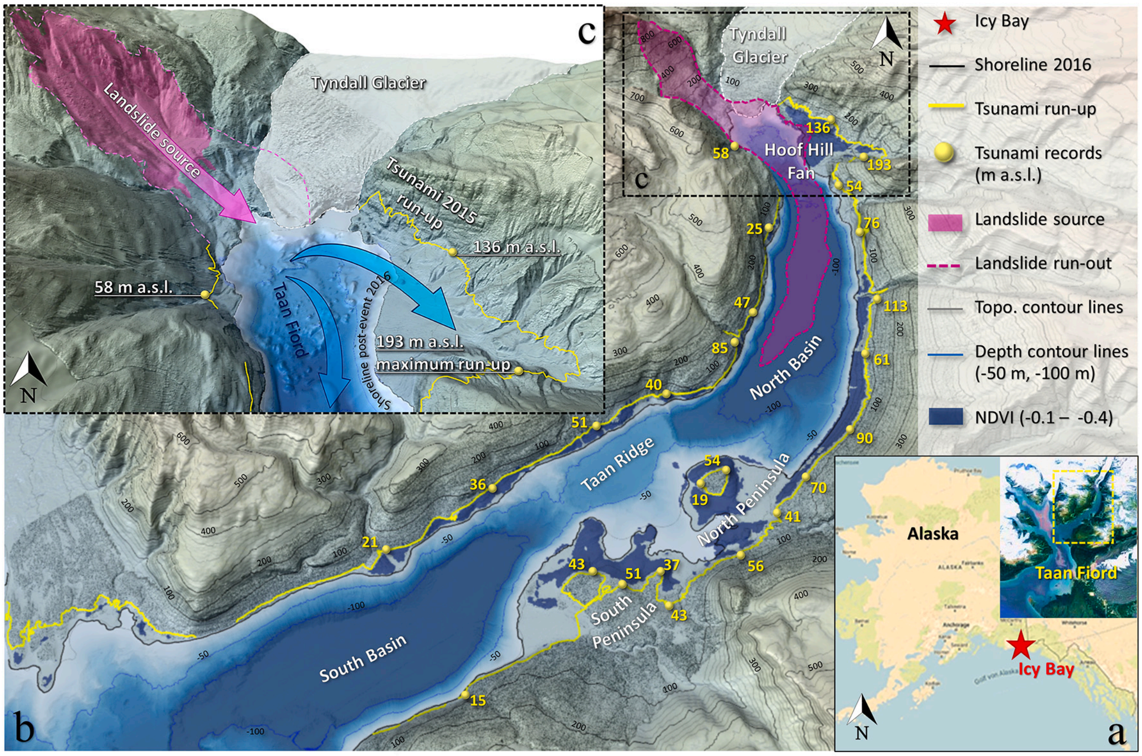

Fig. 1. a) Location of Icy Bay and Taan Fiord, southern Alaska. b) View of Taan Fiord in 2012 and tsunami run-up (DEM 2012 provided by Elevation Portal of Alaska – DGGS, and DEM 2016 from Haeussler et al., 2018). NDVI in the legend indicates the *normalized difference vegetation index*, highlighting the forest destruction (Cannon, 2017). c) Impact area and landslide source at the head of the fiord, the maximum run-up of 193 m a.s.l. is located at the Hoof Hill Fan location. Coordinate reference system: Universal Transverse Mercator WGS84/UTM zone 7 N (EPSG: 32607).

amplitude) of 100 m a.s.l., which propagated and reached the mouth of the fiord in around 12 min, featuring a maximum run-up of 193 m at the Hoof Hill Fan location, in front of the landslide source (Dufresne et al., 2018; Haeussler et al., 2018; Higman et al., 2018). Out of the impact area, the run-up ranges from 40 to 113 m a.s.l. and decreases to around 10–30 m a.s.l. towards the mouth of the fiord (Fig. 1). An inundated area of more than 20 km^2 was observed (Higman et al., 2018) resulting in significant forest devastation and soil erosion.

Before the 2015 event, the Taan Fiord had been extensively studied, since significant and rapid geomorphological changes were attributed to the fast retreat of the Icy Bay glacier in the last century (Meigs and Sauber, 2000; Meigs et al., 2006; Koppes and Hallet, 2006). After the stabilization of the Tyndall Glacier at the Taan Fiord head, at its terminus around 1991 (Williams and Koppes, 2019; Bloom et al., 2020), a huge landslide body was recognized on the west flank of the fiord, where scarps have been reported from aerial photos taken in 1996 (Meigs et al., 2006).

George et al. (2017) numerically modeled the 2015 tsunami event at Taan Fiord adopting a new single-layer and multiphase depth-averaged model. They recreated most of the features of the landslide process (with a total volume of 78 Mm^3) and the wave dynamics starting from their reconstruction of the pre-event sliding surface, the fiord head, and the bathymetric surface. Dufresne et al. (2018) and Higman et al. (2018) provided the results from detailed field investigations. They defined the landslide as a rotational “slide block”, made of weakly lithified sandstone, and described the wave dynamics observing geological records onshore after the event, which permitted the identification of the entire inundated area following the trimline (defined by “chopped trees”) and new sediment deposits further onshore. Additionally, they observed the presence of landslide material onshore with grain diameters that vary extremely from tens of cm up to 20 m blocks. Haeussler et al. (2018) provide the results from geophysical investigations (multibeam bathymetry, Lidar - Pulsed Scanning Altimeter, and high-resolution multichannel marine seismic profiles) that took place in summer 2016, focusing on topographical changes, bathymetric observations, and seismic stratigraphy for submarine depositional processes. Apart from several blocks (up to 35 m in width), they observed a large block about 300 m in diameter on the bay floor, with a more rounded morphology. They suggested that this could consist of sediments (like part of the fiord-floor sediments that might have been displaced southward) rather than of a single sedimentary rock from the slide source outcrop. Further, they describe the fiord bathymetry before October 2015 and estimate an infill of the northern fiord of about 70 m in thickness after the 2015 event. They provided a volume estimate for the subaerial source of about 75.7 Mm^3 by comparing their DEM with the InSAR DEM of 2012. Gualtieri and Ekström (2018) provide a broad-band seismic analysis and modeling of the seismic signal recorded while the landslide collapsed at the Taan Fiord, from which a mass of 150 million metric tons has been estimated, equal to a volume of about 55 Mm^3 for a given rock grain density (ρ_g) of 2700 kgm^{-3}. Williams and Koppes (2019) described the geomorphic dynamics of the fiord with the Tyndall Glacier retreat and the recent formations of new sediment supplies in the fiord. Bloom et al. (2020) reported drastic morphological changes in the fiord due to erosional wave processes on the coastline, with a focus on fans and deltas modifications after the tsunami event in October 2015. They stated that the front of a few deltas, close to the slide source, collapsed because of the toe erosion due to landslide subaqueous run-out during the tsunami event, contributing to the fiord floor infill.

2. Data and methods

The main goals of the geomorphological analyses are i) to describe the landslide dynamics and to establish possible relationships with the glacier movements utilizing open-source GIS software (QGIS); ii) to quantify the volumes involved in the displacements before the final collapse and the one that induced the tsunami on October 2015; iii) to define a database of the governing parameters, useful for the further numerical simulations.

Since the modeling focuses on wave dynamics, the physical landslide reconstruction (subaerial sliding process and submerged mass transport) is not the goal of this research. The task is to reproduce a similar impact process in initiating the impulse wave, where the adoption of different modeling approaches with comparable impact intensities is evaluated in Flow3D.

2.1. Available digital elevation models

Several DEMs from 2000 to 2016 have been compiled (available from different sources, see Table 1). The Elevation Portal of Alaska – DGGS (Discrete Global Grid System) provides DEMs for the Icy Bay area, from 2000 to 2014. A reconstructed, pre-collapse model of the Taan Fiord head and bathymetry from October 2015, based on the IFSAR DEM of 2012, is available from the work of George et al. (2017). Since 2017, a new dataset for the Icy Bay (Arctic DEM AK V.2–2014) is available on the Elevation Portal of Alaska – DGGS, giving the possibility to observe the landslide position one year before the catastrophic event and to update the estimate of the landslide volume before the final collapse. Haeussler et al. (2018) produced a detailed bathymetry and topographic surface (DEM of 1-m grid resolution) of the fiord after the tsunami event.

Since the Arctic DEM-2014 shows significant vertical (and also horizontal) offsets compared to the DEMs of 2012 and 2016, a co-registration (correction in offset differences) for the digital models of 2014 and 2016 to the DEM of 2012, using the method presented by Nuth and Kääb (2011), was performed. A collection of python and shell scripts for DEM co-registration ("demcoreg", Shean et al., 2016) was used. Afterwards, a Root Mean Square Difference (RMSD, obtained for "stable terrain features" present in the DEMs) between the DEMs of 2014 and 2012 and between 2016 and 2014 was found to be 2.03 m and 1.85 m respectively. Considering the high geomorphological dynamics in this area and the high variability in snow cover during the year, these statistical parameters seem to be reasonable indicators for this study.

2.2. Data, bathymetry, and topography reconstruction

According to Higman et al., (2018), considering a water depth of 100 m at the fiord head in front of the Tyndall Glacier and a maximum run-up of 193 m a.s.l., the wave crest is estimated to reach about 100 m a.s.l., with a period of 90 s, before breaking and reaching the Hoof Hill Fan as a surging breaker. Additionally, a propagation speed of about 30 ms^{-1} is estimated. With a *"simple conversion of kinetic to potential energy usually used to estimate flow velocity from run-up height"* (see Dufresne et al., 2018; Higman et al., 2018) the sliding speed is empirically estimated to be in a range of 36–45 ms^{-1}. The landslide material is composed mostly of weak lithified sandstones, whose grain density ranges between 2150 and 2650 kgm^{-3} with an average of 2350 kgm^{-3} (Hackett, 1976). Some slide material did not enter the fiord but remained on the glacier and the bottom of the scar. In the work of Haeussler et al. (2018) this remaining debris is calculated to be approximately 1.5 and 21.9 Mm^3 respectively. Gualtieri and Ekström (2018) estimated the duration for the sub-aerial sliding process to be roughly 90 s, where the center of mass (at an elevation close to 340 m a.s.l. for a mass of 150 million tons) accelerated significantly in the first 30 s while decelerating in the last 60 s, with motion primarily in the *E*-W direction and a smaller N-S component.

New additional data like the remobilized landslide volumes were generated employing the geomorphological analysis and DEMs elaborations.

The pre-event 2015 bathymetry (See Data Availability) and topography are reconstructed based on the DEM provided by Haeussler et al. (2018) and the 2012 InSAR DEM. To recreate geomorphological elements as they were in October 2015 (e.g. the coastline, the shape of the Hoof Hill Fan, the location of the Tyndall Glacier, and the sliding surface for the landslide), the Arctic DEM AK V.2–2014 and the DEM of George et al. (2017) are used. The pre-event bathymetric surface in the impact region is replicated considering the model proposed by George et al. (2017) which corresponds to the bathymetric map of Meigs et al. (2006). Additionally, interpreted seismic reflection cross-section images and calculated isopach maps of the seismic stratigraphic units provided by Haeussler et al. (2018), allow recreation of the upper fiord depth (about 160 m) before the landslide collapse. Finally, solid bodies regarding pre-event topography and bathymetry are developed and exported to stereolithography (STL) files using the Rhinoceros 6 software (see Data Availability).

2.3. CFD code Flow3D

The finite-volume-based CFD software Flow3D is used to numerically model the flow dynamics (Harlow and Welch, 1965; Welch et al., 1968; Nichols et al., 1981). The code can model two-fluid problems, where all velocity components (u, v, w) are computed in the 3D domain, addressing the Reynolds-Averaged Navier-Stokes Equations (RANS, Hinze, 1975), implementing the Fractional-Area/Volume-Obstacle-Representation (FAVOR, Hirt and Sicilian, 1985) and the Volume-of-Fluid methods (VOF, Nichols et al., 1981, Rady, 2011).

To compute turbulences and viscosity issues in Flow3D, the renormalized group model (RNG)-based K-epsilon turbulence model (k-ε) is utilized (Yakhot and Smith, 1992), which uses statistical formulations to compute the turbulent kinetic energy dissipation rate (Harlow and Nakayama, 1968; Chung, 2010; Ersoy et al., 2019).

In Flow3D, a surface roughness parameter (R_r), defined as equivalent grain roughness (or absolute height in meters) can be set for every solid-

Table 1
Summary of the Digital Elevation Models (DEM) used for the analysis and related information. Reference system from the EPSG register (*European Petroleum Survey Group*).

DEM CATALOG - ICY BAY - TAAN FIORD						
Name	Pubblication Date	Acquisition Date	Resolution (m)	Method	EPSG	Source
Icy Bay 2000	30/08/2000	18–26/08/2000	5	Intermap STAR-3i airborne interferometric synthetic aperture radar (SAR) system mounted in a LearJet 36A aircraft.	32,607	DGGS Elevation Portal of Alaska
Mt Saint Elias 2002	30/12/2002	03–05/08/2002	10	Intermap Technologies airborne interferometric SAR data acquisition system.	32,607	DGGS Elevation Portal of Alaska
IFSAR	08/04/2015	14/08–08/09/2012	5	InSAR data	3338	DGGS Elevation Portal of Alaska - USGS National Map
Arctic DEM AK (5 m Mosaic) V2	21/05/2017	01/03/2014	5	Optical stereo imagery, high-performance computing, and open source photogrammetry software.	3413	DGGS Elevation Portal of Alaska
taan_topobathy_1m_UTM7_WGS84	11/10/2018	01/05/2016	1	Lidar data set, collected using a system based on a Riegl LMS-Q240i Pulsed Scanning Altimeter	32,607	Haeussler et al. (2018)

body included in the model domain, allowing for the effects of vegetation, grains, or geomorphological discrepancies that are not reproduced by the STL file on the flow dynamics to be considered.

Different approaches to model fluid-like volumes have been used to reproduce sliding-impact processes (Basu et al., 2009; Gabl et al., 2015; Ersoy et al., 2019). For this work, both the dense fluid (Franco et al., 2020) and granular media models (Alvarez and Wendelbo, 2018) are adopted for the wave initiation at Taan Fiord.

Adopting a Newtonian-like denser fluid relative to the sea water density, to model a sliding body, is an easy and suitable approach for gravitational processes which behave as fluid while running down a slope (Franco et al., 2020). The implementation of this concept is not recommended to accurately reproduce a sliding process like the one at Taan Fiord in October 2015, but it can be used as a well-adapted approximation to qualitatively recreate the impacting volume of the slide that entered the Fiord (Franco et al., 2020). Regarding density calculations in the models, the second-order approach for the density evaluation (Flow Science Inc, 2020) is applied to accurately consider the interaction and mixing between the denser fluid and sea water.

The simplified application of the granular flow model in Flow3D is treated as a non-Newtonian fluid like a one-phase continuous fluid in which the combination of fluids and particles is referred to as a slurry, commonly used to recreate debris flow processes (Hirt, 2010, 2013). This mixture is treated as an incompressible fluid that may be linked to free surfaces, referring to a high concentration granular media featuring a volume fraction of the granular content equal to or greater than 50% (Bagnold, 1941; Mih, 1999).

3. Geomorphological analysis

3.1. Glacier migration and landslide displacements

From the interpretation of the different DEMs (Table 1) and additional data sources as Landsat 7 and 8, it is observed that the Tyndall Glacier front at the head of the fiord had advanced and retreated several times in the last decades (Fig. 2a,b), also confirmed by Williams and Koppes (2019). Along section G-G' the glacier front advanced more than 500 m from 2000 to 2012 (Fig. 2c). After its greatest advance in 2013 (about 750 m), the front retreated again by approximately 500 m in 2014 and another 150 m up to the time of the documented landslide in 2015. As reconstructed by George et al. (2017), in October 2015 the glacier is very close to the 2000 location. After the event in 2016, the

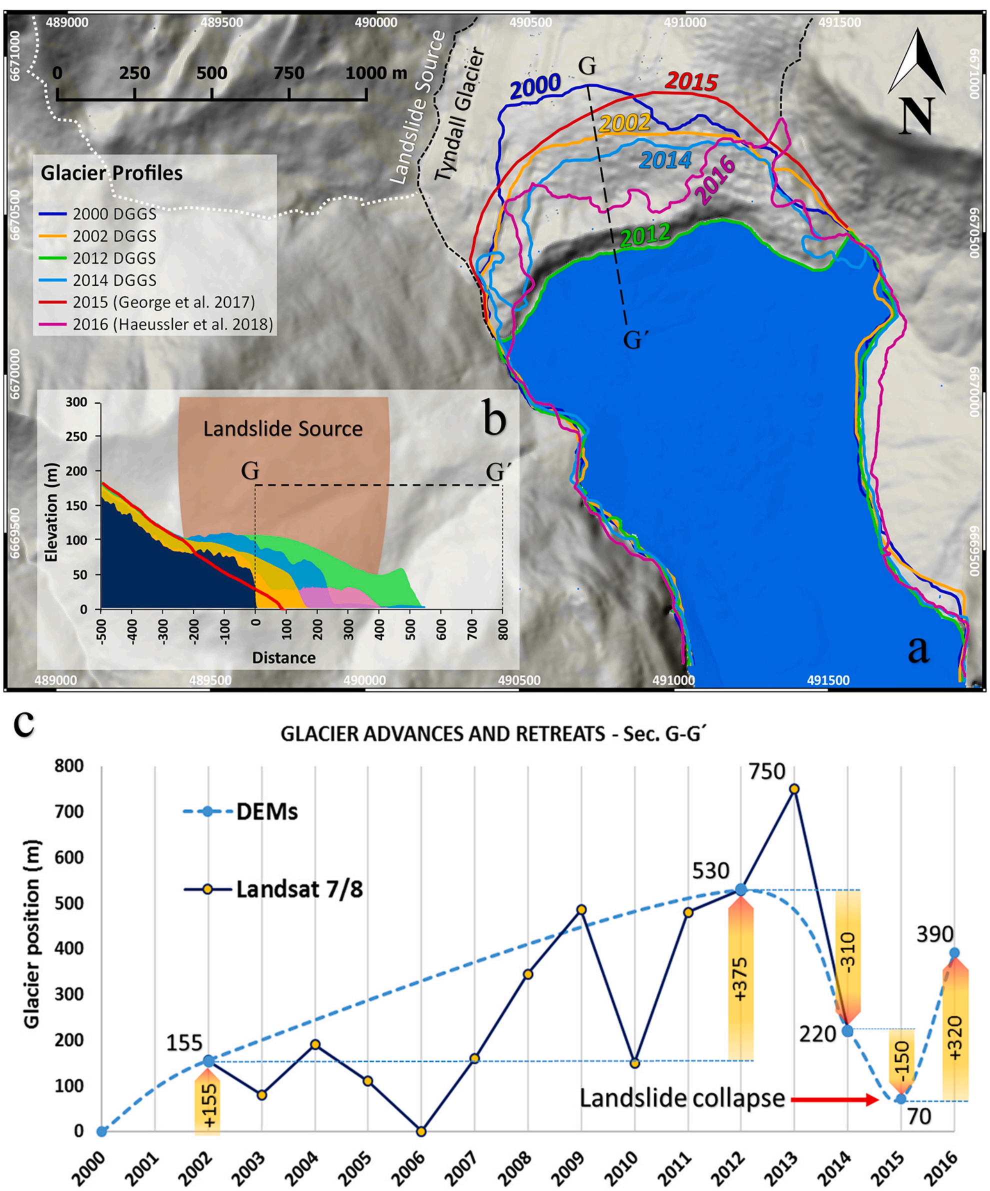

Fig. 2. Coastline changes in time at the fiord head. a) The variation in the glacier and the delta fronts are reconstructed for 2000 to 2016. The Coastline and glacier position of 2015 is taken from the reconstruction of George et al. (2017) as the fiord head pre-event configuration (red line). The dotted white line shows the landslide source; the black dotted line isolates the glacier body. b) Glacier position in time, on a vertical section, concerning the landslide source. c) Glacier position in time for the available DEMs and satellite images from Landsat 7 and Landsat 8 - USGS. Orange columns highlight the associated glacier movement rate, along the section G-G`, based on the available DEMs. (For interpretation of the references to colour in this figure legend, the reader is referred to the web version of this article.)

glacier advanced again by approximately 320 m.

Landslide displacements can be related to these glacier movements. In Fig. 3b several upslope facing scarps present from 2000 to 2014 are highlighted, with variable horizontal displacements of 30–100 m in the slide direction. Grabens in the upper part of the landslide body are present in the year 2000 (black arrows in Fig. 3); these were previously noticed on aerial photos taken in 1996 (Meigs et al., 2006). Vertical offsets along cross-section A-A′ (Fig. 3 bc) at distances of 500–750-1000 m from the landslide crest are estimated to be −47 to −67 m and − 33 – −76 m for the intervals 2012–2014 and 2014–2016 respectively. Such large vertical offsets can be attributed to the presence of sub-vertical discontinuities or listric faults in the slide body (black dashed lines in Fig. 3) that intersect the sliding surface (red dashed line in Fig. 3) defined by George et al. (2017).

Mass movement area, elevation difference distributions, and related volumetric changes are obtained through a raster difference utilizing the raster calculator tool in QGIS (Fig. 4). Between 2000 and 2002 (Fig. 4a) maximum, vertical displacements of maximum −15 m on the upper part of the slide body and small increases in the center are noticed while the glacier advanced, maintaining a thickness of 70 m. In the time interval from 2002 to 2012, larger displacements are recognized in the upper part of the landslide with a maximum negative offset of −40 m and a maximum positive offset of about 25 m (Fig. 4b). In 2012 the glacier

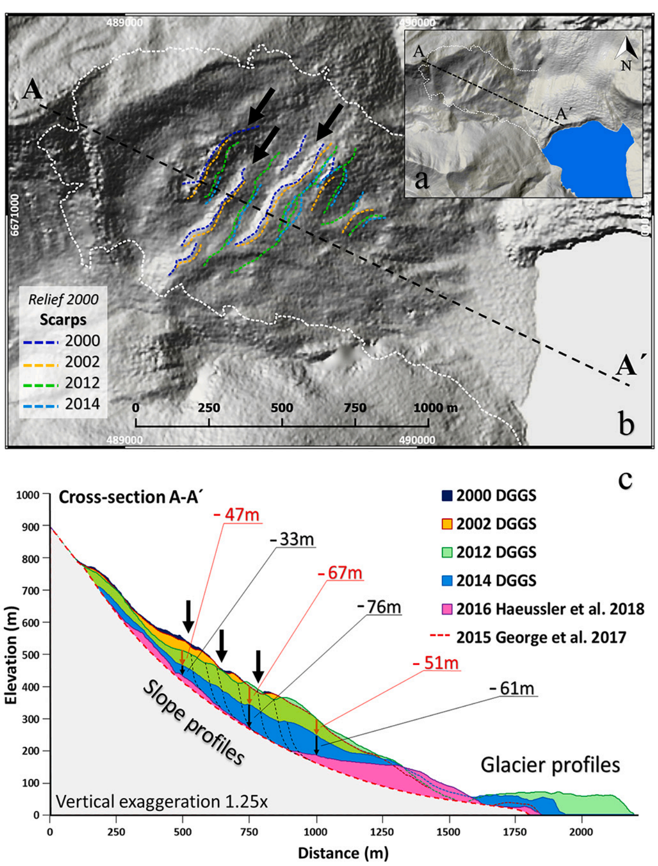

Fig. 3. a) Position of cross-section A-A′ to the landslide and the glacier bodies (relief of 2012 refers to Fig. 2a). b) Recognized scarps in the landslide area (white dashed line) from 2000 to 2016. The black dashed line represents the cross-section A-A′. b) Different slope profiles in time along section A-A'. Vertical displacements between 2012 and 2014 (red) and 2014–2016 (black) are estimated. The black arrows indicate the position of the observed grabens. Sub-vertical listric faults (black dashed lines) in the landslide body are hypothesized as a result of the presence of scarps and considerable vertical displacements. The red dashed line shows the failure surface reconstructed by George et al. (2017). (For interpretation of the references to colour in this figure legend, the reader is referred to the web version of this article.)

reached a thickness of 90 m. Between 2012 and 2014 a considerable displacement is noticed (Fig. 3, 4c), with a maximum vertical offset of −90 m resulting in about −28.5 Mm^3 change of volume (Table 2, Fig. 4c, area in the green line). At the base of the landslide and on the glacier (that retreated about 500 m from 2013 with a reduction of −60 m in thickness at the head of the fiord) a positive volume change (Fig. 4c, area in the yellow line) resulting in an additional volume of 3.5 Mm^3 (Table 2), which is up to 35 m in thickness, can be observed.

The exported volume from the raster difference between the years 2014 and 2016 results in approximately −27.5 Mm^3 (Table 2), where maximum negative vertical displacements are estimated in the range of −105 m (Fig. 4d, area in the green line). Additionally, accumulated material with a thickness up to 35 m (Fig. 4d, area in the yellow line) is still observed in the slide scar, resulting in 1.75 Mm^3 (Table 2). According to George et al. (2017), the glacier had a varying thickness between 50 and 20 m in front of the slide source from north to south at the moment of the collapse. Afterwards, the glacier results completely disintegrated from the landslide.

3.2. Landslide dynamics

Slope stability seems to be influenced by glacier movements together with the evolution of the defined discontinuities (Fig. 3 c) since several displacements are noticed while the glacier advanced and retreated. From the literature review (section 1) and the presented outcomes from geomorphological analyses (section 3.1), a plausible interpretation regarding the landslide dynamics, from its initiation until failure, is proposed. Four main stages are defined (Fig. 5):

1) Before 1983, when the ice occupied most of the fiord, the glacier had an elevation of about 450 m a.s.l. at the location of the landslide (Fig. 5a) (Meigs and Sauber, 2000). The fast retreat and the ice loss might have induced slope instability on the west flank of the fiord head, with the consequent formation of counter slope scarps and antithetic discontinuities (or local normal faults) inside the new slide body. This was already assumed by Meigs and Sauber (2000), referring to the year 1996, with a dip angle ranging between 60 and 80° facing against the slope (Fig. 5a).
2) Given this and the hypothesized sub-vertical discontinuities (as shown in Fig. 3), it can be assumed that the landslide body has rigidly rotated counter clockwise on average 20° - 30° while sliding downslope in the last decades (Fig. 5b), where deformations occurred due to displacements along the discontinuities.
3) Therefore, the rotation of the slide body might have reversed the relative direction of motion along these discontinuities (Fig. 5c). After the discontinuities reached a sub-vertical dip angle, developing further in the above-mentioned listric faults (section 3.1), a resulting sudden and significant vertical displacement was observed after 2012, possibly further decreasing the stability of the slope. This interval could represent an important phase of the creeping motion of the landslide. Caused by the large displacement, the pressure at the base might have induced a bulge of part of the glacier just in front of the sliding body (Fig. 4c, yellow area on the glacier side, and Fig. 5c). This remarkable stage of landslide dynamics can be additionally explained based on the assumption of existing deeper sliding surfaces (dashed red lines in Fig. 5), not necessarily the one where the landslide failed (full red line in Fig. 5d); or similarly, considering the presence of multiple sliding surfaces, forming a thick shear zone (Fig. 5c, d). This assumption is also stated in Meigs and Sauber (2000) where they report uncertainty regarding the depth of the fiord bottom in front of the landslide source (Fig. 5a).
4) Triggering the final collapse, the sudden glacier retreat after 2013, the lack of ice thickness in front of the sliding mass (thus a missing lower slope buttress), and the enucleation of a shallower sliding surface (Fig. 5c, d), might have destabilized the slope, resulting in the catastrophic event.

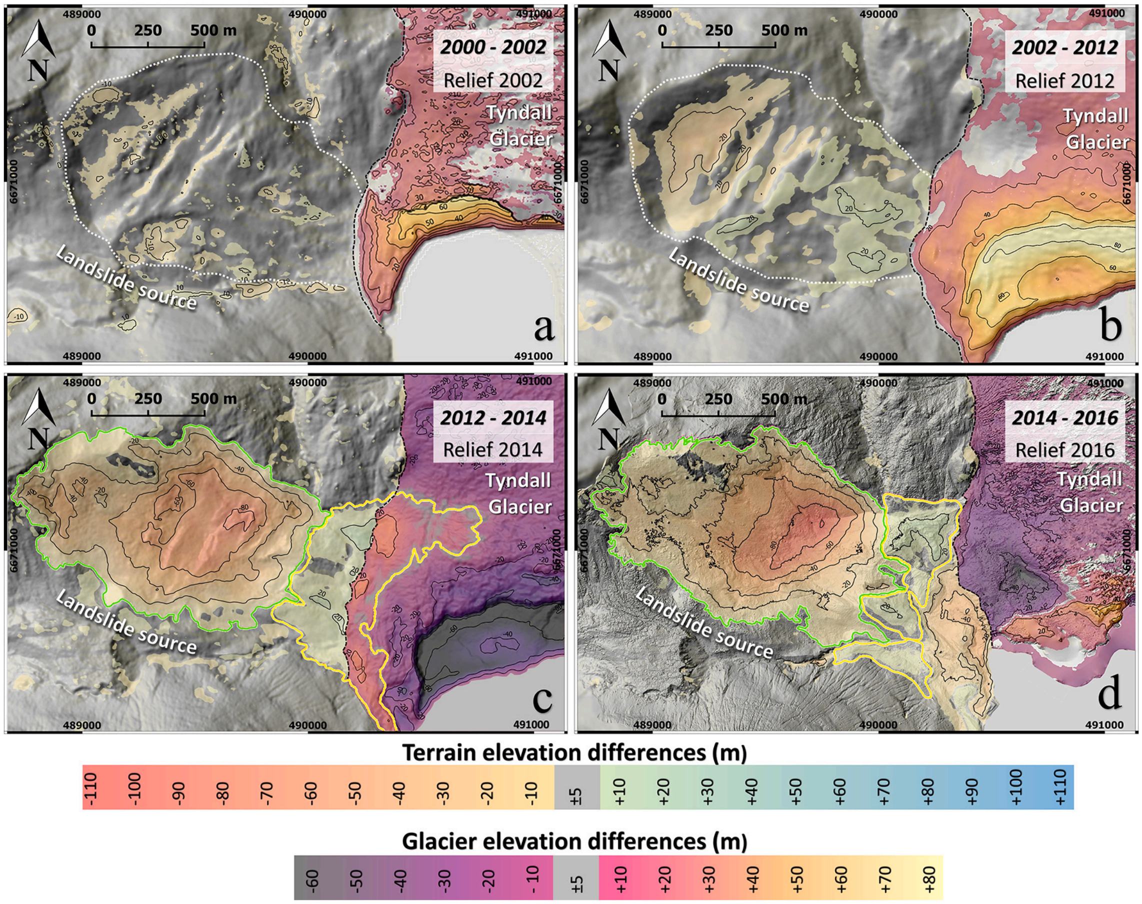

Fig. 4. Landslide and glacier evolution and involved displacements distribution. The difference in elevation for the landslide area and glacier body are shown for the time intervals a) 2000–2002, b) 2002–2012, c) 2012–2014, and d) 2014–2016 represents the final collapse. The white dotted line in a) and b) isolate the portion of slope (the landslide source) mostly interested by initial displacements; the black dashed line separates the landslide source from the glacier body. Green and yellow lines in c) and d) refer to areas with negative and positive vertical changes. (For interpretation of the references to colour in this figure legend, the reader is referred to the web version of this article.)

Table 2
Volumes and related area extent for the landslide displacement for the time intervals 2012–2014 and 2014–2016. Deviations are estimated by multiplying the RMSD-based error for the related positive and negative area changes.

Time interval	Resolution (m)	NegativeΔV (Mm^3)		Mapped area (m^2)	Positive ΔV (Mm^3)		Mapped area (m^2)
2012–2014	5	*−28.50*	*± 1.66*	*817,000*	*3.51*	*± 0.76*	*373,000*
2014–2016	5	*−27.50*	*± 1.52*	*824,000*	*1.75*	*± 0.34*	*183,000*

Moreover, as reported in Higman et al. (2018), in September and October 2015 precipitation records at the gauge in Yakutat (110 km away) were about 10% higher than the long-term average. Even though these deviations were noticed in the years before the landslide collapse, rain events combined with the fast glacier retreat could have influenced the underground water table and water saturation inside the landslide body. Notably, one more hypothesis refers to a remote earthquake (4.1 M_w) that happened about 500 km from the Taan Fiord. Seismic waves arrived at the fiord 2 min before the slide collapse (Higman et al., 2018). Despite the distance, the waves could have induced a small but still significant fluctuation in the pore pressure inside the landslide body, reducing its stability until failure.

3.3. Estimation of landslide volume and governing parameters

Haeussler et al. (2018) estimated a volume remaining on the shore of about 23.4 Mm^3 (Table 3). Combining these values with the findings in this work (Table 2), the total volume involved in the final collapse is estimated to be approximately 49.4 Mm^3 (Table 3). While this is the total amount of material involved in the landslide, 26.0 Mm^3 entered the fiord, possibly triggering the tsunami (Table 3).

Previous studies calculated a much higher slide volume (about 75.7 Mm^3) based on the difference in the digital elevation models of InSAR DEM 2012 and the DEM 2016 provided by Haeussler et al. (2018). So far, the estimate of the total remobilized volume in this work (49.4 Mm^3), calculated with the raster difference between the Arctic DEM AK V.2–2014 and the DEM 2016 (Haeussler et al., 2018), is the nearest to that obtained by the works of Gualtieri and Ekström (2018), approximately 55 Mm^3. This supports the volume estimate resulting from this analysis as being realistic for the landslide at the Taan Fiord.

The length along the slope is approximately 1630 m, the width is nearly 915 m, the maximum thickness is 93 m and the maximum depth of the sliding surface is 105 m. The landslide body ranges from an elevation of about 60 m a.s.l. at the toe to 830 m a.s.l. at the crown (Table 3).

Considering the landslide position after March 2014 and the glacier

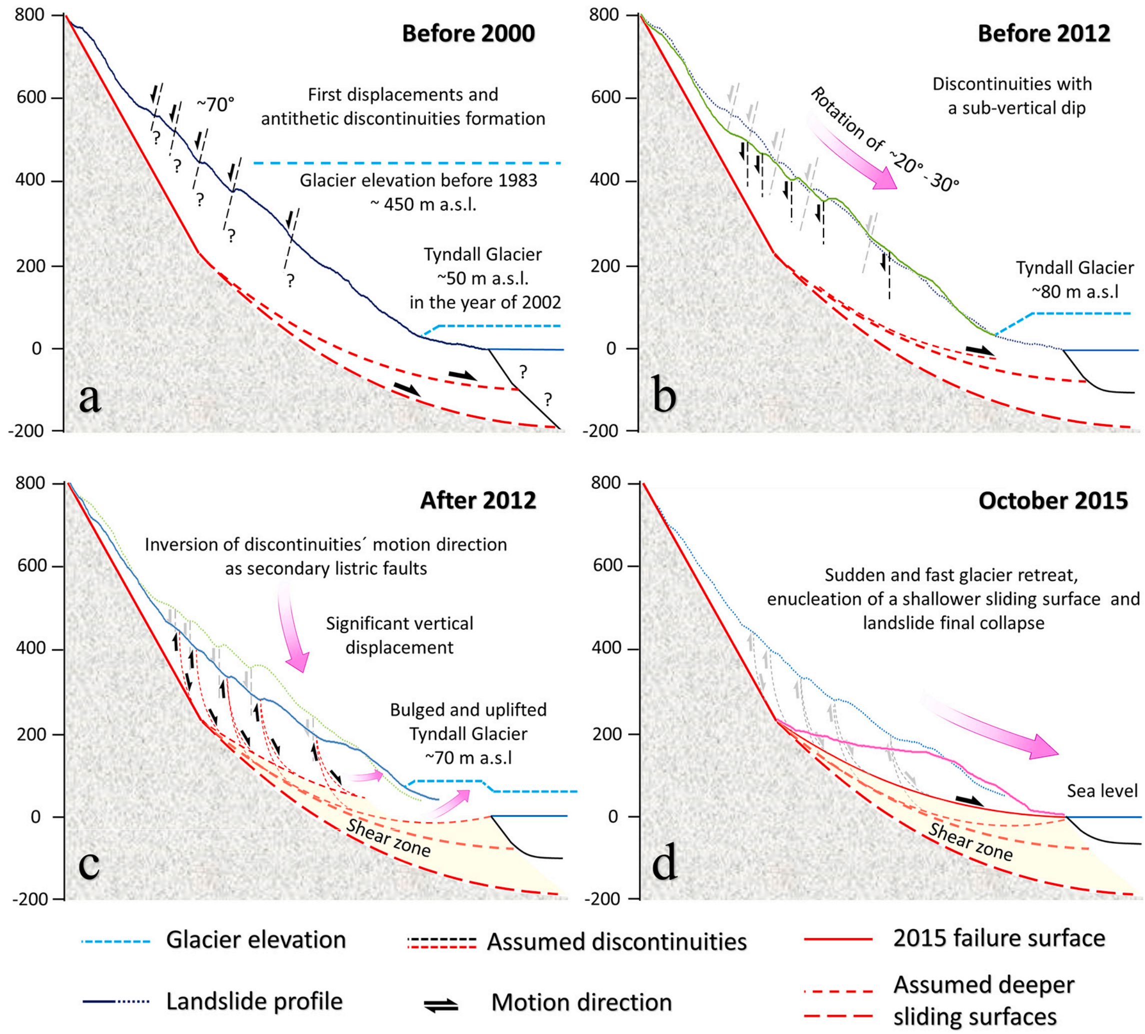

Fig. 5. Interpretation of the landslide dynamics in the last decades and the evolution of the sliding surface. a) First displacement of the landslide as a response of the glacier retreat with the formation of antithetic discontinuities (info from Meigs and Sauber, 2000). b) The landslide rotation brings the discontinuities to a sub-vertical dip. c) Inversion of the direction of motion along the discontinuities, evolving as listric faults and inducing a significant vertical displacement of the landslide body and an upward bulge of the glacier at the toe. d) With the enucleation of a shallower sliding surface, the landslide body fails and collapses, disintegrating the glacier.

position in 2015, it is plausible that the landslide, while entering into the water body, acted like a sub-horizontal piston (10–20° slope, Table 3), disintegrating a part of the glacier, inducing the wave by impacting the fiord with a speed estimated between 36 and 45 ms^{-1} (Table 3, Dufresne et al., 2018; Higman et al., 2018).

Since no geotechnical investigations have been carried out so far, the rheology of the landslide at Taan Fiord is unknown. The slide phase might be referred to as a mixture of different components (soil, rock, vegetation, and snow), thus to a non-Newtonian viscoplastic fluid model as a deformable slide mass.

In addition, the angle of repose, which describes the maximum resting angle of the slide material (assumed as a granular medium), is estimated to be on average 34° by observing the inclination of the remaining debris deposited in the upper part of the scar. Given this value, the angle of friction φ_g for the granular material can be assumed to be 2° to 8° higher than the repose angle (Witt, 2017) ranging between 36 and 42° (Table 3).

From the findings of these geomorphological analyses and the review of previous literature (section 2.1), a database is compiled, summarizing the main governing parameters regarding the landslide properties, the collapse phase, and the estimated wave characteristics (Table 3). These data provide a base for the further numerical models in this study. Additionally, it is understood that after the failure, the frontal part of the slide did not disintegrate significantly while sliding downslope and impacting the fiord and the glacier (mostly maintaining its volume). The further remaining subaerial portion of the landslide disintegrated, partly running over the front of the Tyndall glacier and accumulating in the lower scar area.

4. Set-up of the numerical model

4.1. Model concepts for the impact process and the wave initiation

In Flow3D, fluid-like models can be utilized to qualitatively reproduce the volume that a water body and the impacting process that triggered the impulse wave.

In the first approach, using the dense fluid model (hereafter labeled "D·F.") with the total volume of the landslide (49.4 Mm^3) might induce the whole mass to enter into the fiord, leading to an overestimation of wave characteristics and inundated area. However, only the volume which completely entered into the water body (26 Mm^3), should be considered. This has been manually defined following the contour lines on the topographic surface, where the upper limit is close to the height of the center of the slide mass (about 340 m a.s.l.,). Usually, a sliding

Table 3
List of the parameters and information based on literature review and estimated in this work.

Data	Symbol	Dimension	Value	References
Landslide crown elevation	–	m a.s.l.	*830*	From this study
Heigth difference between slide crown and toe	L	m	*765*	From this study
Landslide width	W_d	m	*915*	From this study
Landslide slope length	L_d	m	*~1630*	From this study
Landslide max. Thickness	S	m	*93*	From this study
Max. depth of the sliding surface	D_r	m	*105*	From this study
Landslide centre of mass	–	m a.s.l.	*~340*	Gualtieri and Ekström (2018)
Landslide impact speed	v_s	m/s	*36–45*	Higman et al. (2018), Dufresne et al. (2018)
Duration of the sub-aerial sliding process	–	s	*~90*	Gualtieri and Ekström (2018)
2015 landslide volume onshore	–	Mm^3	*23.4*	Haeussler et al. (2018)
2015 landslide volume entered in the fiord	–	Mm^3	*26.0*	From this study
2015 total landslide volume	V_g	Mm^3	*49.4*	From this study
Impact slope angle	α	°	*10–20*	George et al. (2017)
Grain density (weakly lithified sandstone)	ρ_g	kg/m^3	*2150–2650*	Higman et al. (2018)
Mean grain density	ρ_g	kg/m^3	*2350*	Higman et al. (2018)
Grain diameter (onshore)	d	m	*0.1–20*	Dufresne et al. (2018)
Grain angle of repose	–	°	*34*	From this study
Grain friction angle	φ_g	°	*36–42*	From this study
Maximum run-up elevation	–	m a.s.l.	*193*	Haeussler et al. (2018)
Maximum wave crest elevation	H_w	m a.s.l.	*~100*	Higman et al. (2018)
Mean water depth (impact area)	h_w	m	*~100*	Meigs et al. (2006)

fluid mass is linked to the bulk slide volume and density for a given porosity (Heller et al., 2009; Gabl et al., 2015; Franco et al., 2020). Assuming that the bulk slide porosity is equal to 0 (no pores) for this portion of the landslide, the estimated in-situ volume of 26.0 Mm^3 and the grain density (Table 3) can be used for the fluid density ρ_f in the model. For this volume, the slide thickness is about 75 m on average.

The second approach uses the granular media model (hereafter labeled "G.M.") to replicate the impact process. Moreover, the possibility of implementing the total estimated in-situ volume of the landslide (49.4 Mm^3) is evaluated. In addition to the grain density ρ_g (2150–2350-2650 kgm^{-3}), this model requires other input parameters and the activation of the density evaluation model. As required in the model set-up, fluid density ρ_w and viscosity μ_w, referring to the fluid surrounding the grains, are set in here equal to the sea water conditions (1035 kgm^{-3} and 0.001 Pas respectively). Based on the description provided by (Dufresne et al., 2018) the average grain diameter is subjectively set equal to 1.0 m. The software computes the effective dynamic viscosity for the granular media model, which is defined by Mih's equation (Mih, 1999):

$$\mu_{eff} = 7.8\mu_w\left(\frac{\lambda^2}{1+\lambda}\right) + \rho_g\left(\frac{0.015}{1+0.5\rho_w/\rho_g}\right)\left(\frac{1+e}{(1-e)^{0.5}}\right)(\lambda d)^2\left|\frac{du}{dy}\right| \tag{1}$$

where μ_w and ρ_w are the fluid viscosity and density, ρ_g is the grain density, e is the coefficient of restitution related with the grain impacts, d is the grain diameter, and λ is a ratio between d and S, where S is the average distance between grain centers minus their diameter. In Flow3D the shear rate du/dy is replaced by the magnitude of the strain rate eij, and an e for sand is assumed equal to 0.7 (Flow Science Inc, 2020). This leads to a simplification of Eq. (1):

$$\mu_{eff} = 7.8\mu_w\left(\frac{\lambda^2}{1+\lambda}\right) + 0.066\rho_g(\lambda d)^2|e_{ij}| \tag{2}$$

which refers to a "shear thickening" viscosity.

The friction angle (φ_g) refers to a different value equal to 36°- 38°- 40°- 42° (Table 3). In Flow3D, the friction angle generates "static frictions" that must be overcome before flow may occur. Indeed, a packed volume (the granular media) at rest cannot flow until the slope angle exceeds the friction angle (Hirt, 2010). Once the φ_g is overcome, the flow (and its velocity) is independent of the friction angle, and then it will keep flowing as long as the slope has a higher inclination than the angle of repose (34°). In a slurry model the defined range of φ_g can influence the dispersive pressure (or normal stress, P_d) that acts to adjust the structure of the granular mass and hence the frictional interaction of the debris flow to the basal surface (Bagnold, 1941; Bartelt et al., 2016), where the larger the friction angle the more reduced dispersive pressure:

$$\mathrm{T} = \tan(\varphi_g)\mathrm{P_d} \tag{3}$$

where T is the tangential stress (Hirt, 2013). Under sufficiently high shear stress, the P_d may prevent the granular media from setting and packing (Bagnold, 1941).

Other fundamental inputs for the granular media model, which are connected to the flow characteristics of the solid material, are i) the close packing volume fraction (CPVF) which defines the grain volume fraction threshold at which a flow "freezes", ii) the mechanical jamming volume fraction, which represents the volume fraction of grains above which the flow generates a resistance due to grain-grain collision, and iii) the random loose packing volume fraction which arises when the grains are interacting just enough to sustain their weight under gravity, and therefore no disturbance forces them into closely packed collections. Discrete particles can only be packed at a given limit whose density is less than that of the real solid material. The landslide debris at Taan Fiord can be referred to as a non-uniform (or poly-dispersed) collection, meaning that the volume fraction depends strongly on the grain size distribution and shape, and thus the CPVF can be approximated close to 1 (Donev et al., 2004). When a granular material enters a computational region through a mesh boundary, the density of the solid-fluid mixture ρ_{mx} has to be set, ranging between water density ρ_w and the one given by the chosen CPVF (ρ_{cpvf}), obtained with the following Eq. (4) (Flow Science Inc, 2020):

$$\rho_{cpvf} = \rho_g\,\mathrm{CPVF} + \rho_w\,[1-\mathrm{CPVF}] \tag{4}$$

This initial density ρ_{mx} has a main role in the model set-up since it drives the shear stress computed within the granular media mass, influencing the propagation process of the volume along the sliding surface. A value equal or too close to that of the corresponding chosen CPVF would not allow the mass to move unless for slopes with a steeper inclination than the friction angle. On the contrary, a too-small value makes the mass behave like a liquid. In this study, mixture densities ρ_{mx} ranging between 97% and 95% of ρ_{cpvf} have been adopted, corresponding to initial packing volume fractions between 0.941 and 0.894 (see the table in the Data Availability).

4.2. Wave dynamics modeling

The near and far-field areas are modeled and analyzed separately. Numerical models in the impact area (near field, Fig. 6a) cover a spatial

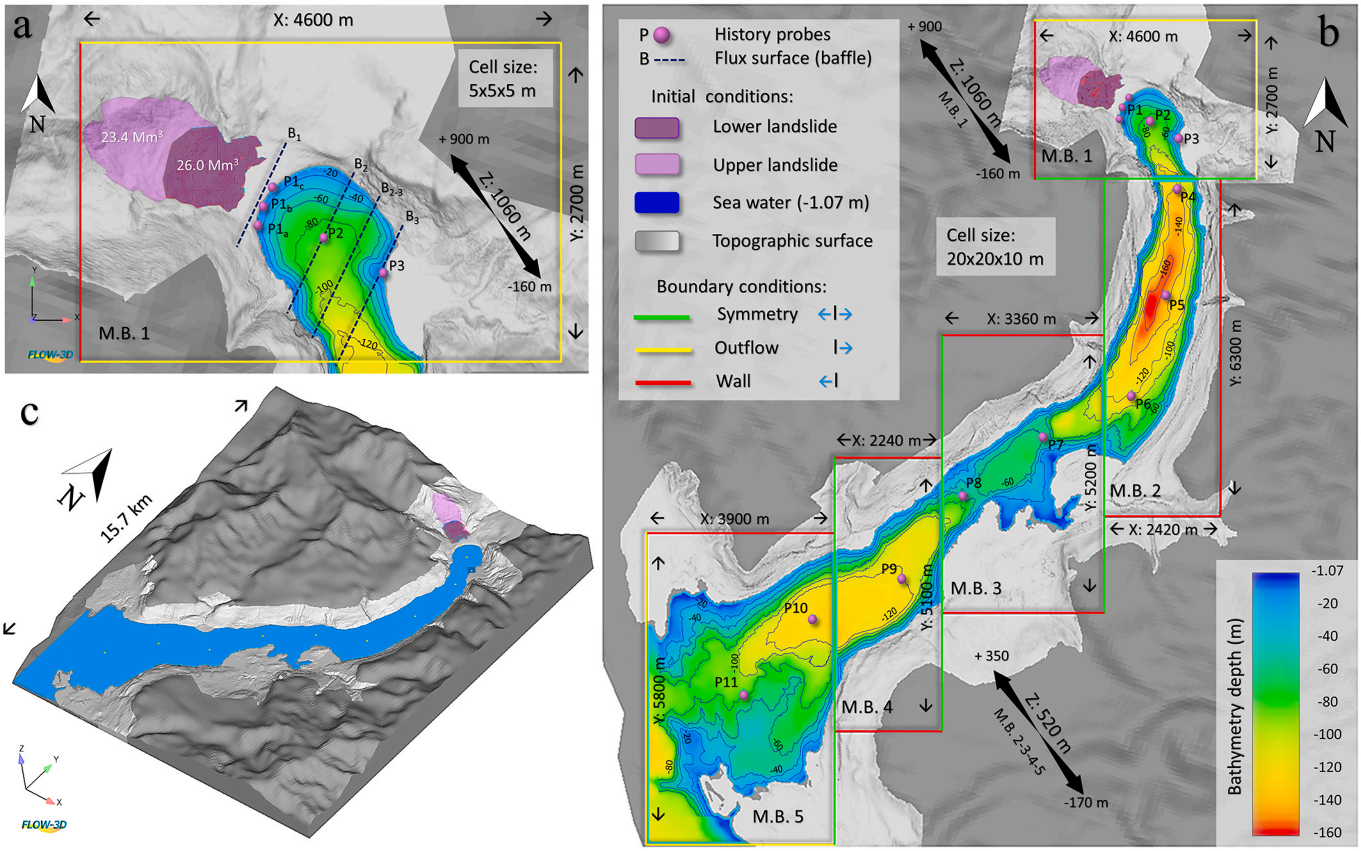

Fig. 6. Set-up for the numerical hydrodynamic simulations for a) the impact area domain (near-field analysis), where one mesh block is used (uniform resolution of 5 m), and b) the whole fiord domain (far-field analysis) where five mesh blocks are adopted (non-uniform resolution of 20x20x10 m). c) Overview of the reconstructed model in Flow3D.

extent of 4600 m × 2700 m in the X-Y direction and 1060 m in the Z direction (from −160 m a.s.l. to 900 m a.s.l.). An orthogonal grid featuring a uniform cell size of 5 m is used. The model domain extent is set so the flow mainly interacts with the solid boundary of the inland slopes and the fiord floor. Boundaries on the free sides of the domain are defined as "Outflow" to avoid any kind of artificial interference or reflection of the fluid (Fig. 6). The volume representing the landslide body, obtained by the raster difference in the DEMs elaborations, is positioned on the reconstructed sliding surface. The initial fluid in the fiord is sea water with a density of 1035 kgm^{-3}.

For tsunami propagation along the fiord (far-field), 5 different mesh blocks are defined (dimensions are expressed in Fig. 6b), where a non-uniform cell size of 20x20x10 m is set. The "Symmetry" boundary condition between each mesh block is set to allow the wave to continually flow from one mesh block to another. To minimize the number of active cells, solid bodies occupy empty cells where no flow is expected, acting as domain limiters.

History probes (or observation gauges) are placed in the domain to record information regarding the impact speed, the impact time, the wave propagation speed, wave crest elevation, and flow speed (referring to the velocity magnitude of a specific point in the 3D system).

In the near field, probes P1a-c, P2, and P3 are set along the direction of the main wave flow (Fig. 6a), for a streamwise distance of 20–650-1340 m respectively from the assumed impact point (located on the coastline just next to P1b, Fig. 6a). For the far-field, additional history probes P4-P11 are placed along the entire fiord (Fig. 6b) with a uniform spacing of 2000 m starting from the impact point.

For this specific case study, the calibration of the slide-related models is intended to replicate a comparable landslide impact intensity, meaning that the sliding body must achieve a similar impact speed entering the water body as documented in the literature (30–50 ms^{-1}). To control the impact speed in those models using the D·F. approach, a surface roughness R_r of 0-1-2m is set for the sliding surface. Additionally, to observe the effects of the topographic surface roughness on the inundation process and related run-up, models with R_r of 1-2-3-4 m for the topographic surface and an R_r of 0.5 m for the bathymetric surface are set.

To validate the wave dynamics models, the intention is to recreate the estimated wave crest elevation of about 100 m a.s.l. after the impact, and the observed run-up with its maximum value at 193 m a.s.l. (Fig. 1c).

Given that the dynamic viscosity of the solid-fluid mixture is already computed with the granular media model, and since this model involves already turbulent flow conditions (Flow Science Inc, 2020), it is not necessary to utilize a turbulence transport model during the stages of impact and wave generation. Accordingly, to simulate the propagation and the inundation process, the turbulence and viscosity model is reactivated once the wave is completely formed, propagating independently from the generation process. Fig. 7 summarizes the model setup for the two proposed modeling concepts.

5. Numerical modeling results

5.1. Impact process and wave generation

To verify the effects of the model parameters on the slide impact and the wave initiation, several simulations were carried out. The D.F. is assumed as a bulk slide volume with porosity close to 0, thus the fluid density ρ_f can be assumed equal to the grain density ρ_g (2150–2350-2650 kgm^{-3}). First observations of the sliding process for the G.M.

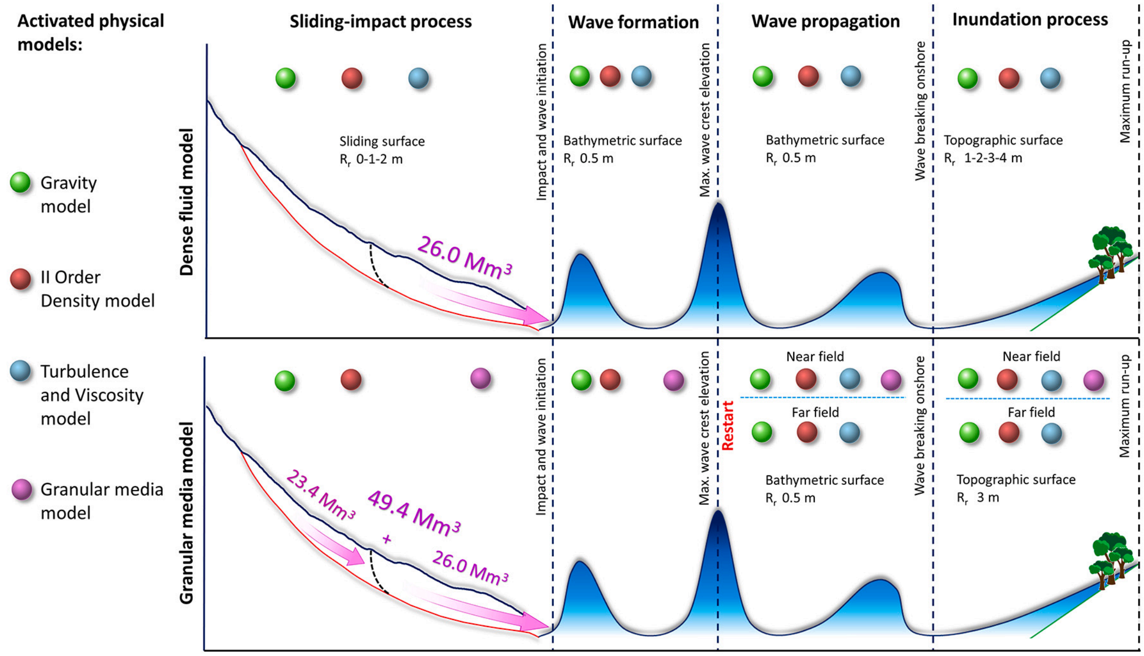

Fig. 7. Activated physical models in Flow3D to simulate the impact process and the wave dynamics for the dense fluid and the granular media modeling approach. Adopted impacting volume and surface roughness R_r (for the sliding, bathymetric and topographic surface) are shown.

suggest the use of a mixture of solid-fluid densities ρ_{mx} of 2032–2220-2502 kgm^{-3} (equal to 95% of ρ_{cpvf}) to best recreate the impact intensity and speed.

A general process description is provided from the impact to the wave detachment and the inundation on the Hoof Hill Fan (see Appendix A. for the history data description). The time step in the simulation will be referred to as "T".

- T 0–16 s: independently from the used model, the sliding mass reaches and impacts the water body within 12–14 s from its release (Fig. 8, 9a).
- T 16–25 s: after the sliding mass enters the water body (with the formation of air cavity effects), the wave is generated (Fig. 9a).
- T 25–35 s: the impulse wave reaches its maximum crest elevation (about 95–99 m a.s.l.) and starts to propagate (Fig. 9 a, d).
- T 35–50 s: the wave flows straight to the opposite shore, impacting and flooding the small delta south of the slide source and the cliff north of the Hoof Hill Fan (with a run-up of 136 m a.s.l., Fig. 1c, 9a).
- T 50–75 s: the wave breaks and runs up the delta and the slopes upon the Hoof Hills Fan, reaching the maximum run-up of 193 m a.s.l. (Fig. 9a).
- T 75–100 s: while the southern slopes upon the delta are flooded directly by the wave, backflow and further reflections inundate the channel east of the delta, representing the farther location from the coastline in the impact area (Fig. 10d).

Depending on the model concept and different combinations of input parameters, differences in results for the sliding-impact process and wave dynamics are found.

In general, for the D.F., it is observed that the R_r of the sliding surface has a significant influence on the impact speed, with maximum values equal to 50.5-43-42 ms^{-1} for an R_r of 0-1-2 m respectively. Similarly, considering depth-averaged flow speed, maximum values of 52-49.5-48.5 ms^{-1} are recorded for an increasing value of R_r (Fig. 9c). An influence is also noticed on the maximum wave crest elevation recorded in P2, varying between 98 and 91.5 m a.s.l. (Fig. 9a, d) where an increase of R_r leads to a decrease of the wave crest elevation. Fluid density ρ_f has no significant influence on the impact speed but slightly influences the wave characteristics in P2. On the contrary, it influences the wave crest elevation recorded in P3 (Fig. 9a, d), where values of 60-63-68 m a.s.l. are observed for a ρ_f of 2150–2350-2650 kgm^{-3} respectively and considering an R_r of 1 m for the sliding surface. This can be explained by the propagation and dispersion process of the D.F. into the water body, thus influencing wave characteristics further from the impact location.

In general, for the G.M., it appears that the φ_g does not influence the impact speed. It might be that in this model the role of grain friction is not directly related to the kinematics of the sliding mass and it does not account for the observed results. Alternatively, the defined φ_g interval, with the massive sliding volume, is insufficiently large to detect substantial changes in the impact process. Generally, the strength of the sliding material along the sliding surface strongly influences the impact speed and the characteristics of the initial triggered impulse wave. Indeed, the grain density ρ_g (which relates to the mixture density ρ_{mx}, Section 4.1) significantly influences the impacting depth-averaged flow speed, resulting in ranges of 34.5–49 ms^{-1}, 33–48 ms^{-1}, 31–47.5 ms^{-1} for ρ_{mx} values of 2150–2350-2650 kgm^{-3} respectively (Fig. 9c). This can be explained with Eq. 2 (Section 4.1), where ρ_g is directly proportional to μ_{eff}. This implies a reduction of the impacting flow speed due to higher resistance to movement of the granular media model with higher dynamic viscosity.

This also implies an influence on the wave crest elevation recorded in P2 (Fig. 9a, d), where maximum values range from 93 to 99 m a.s.l. from higher to lower ρ_{mx}. This does not happen further in P3, where the wave crest elevation stays in the close range of 58–59 m a.s.l. For the wave generated by the D.F. probe P2 represents a good location to analyze the maximum wave crest; the wave generated by the G.M. has its maximum crest elevation slightly to the north of P2, with values of 95–99-101 m. a. s.l. from higher to lower ρ_{mx}.

Through the implementation of flux surfaces (or baffles, dashed lines in Fig. 6a) perpendicular to the flow direction at the impact location and in the wave propagation zone (between P2 and P3), it is possible to estimate the cumulative volume flow rate distribution (Fig. 9b) and the flow momentum (mass in motion estimated as the product of the mass flow rate and the average flow speed) for both the impacting mass and the remobilized water volume (Fig. 9e). When the wave reaches its maximum crest elevation (T 29–31 s), about 20 Mm^3 for the D.F has

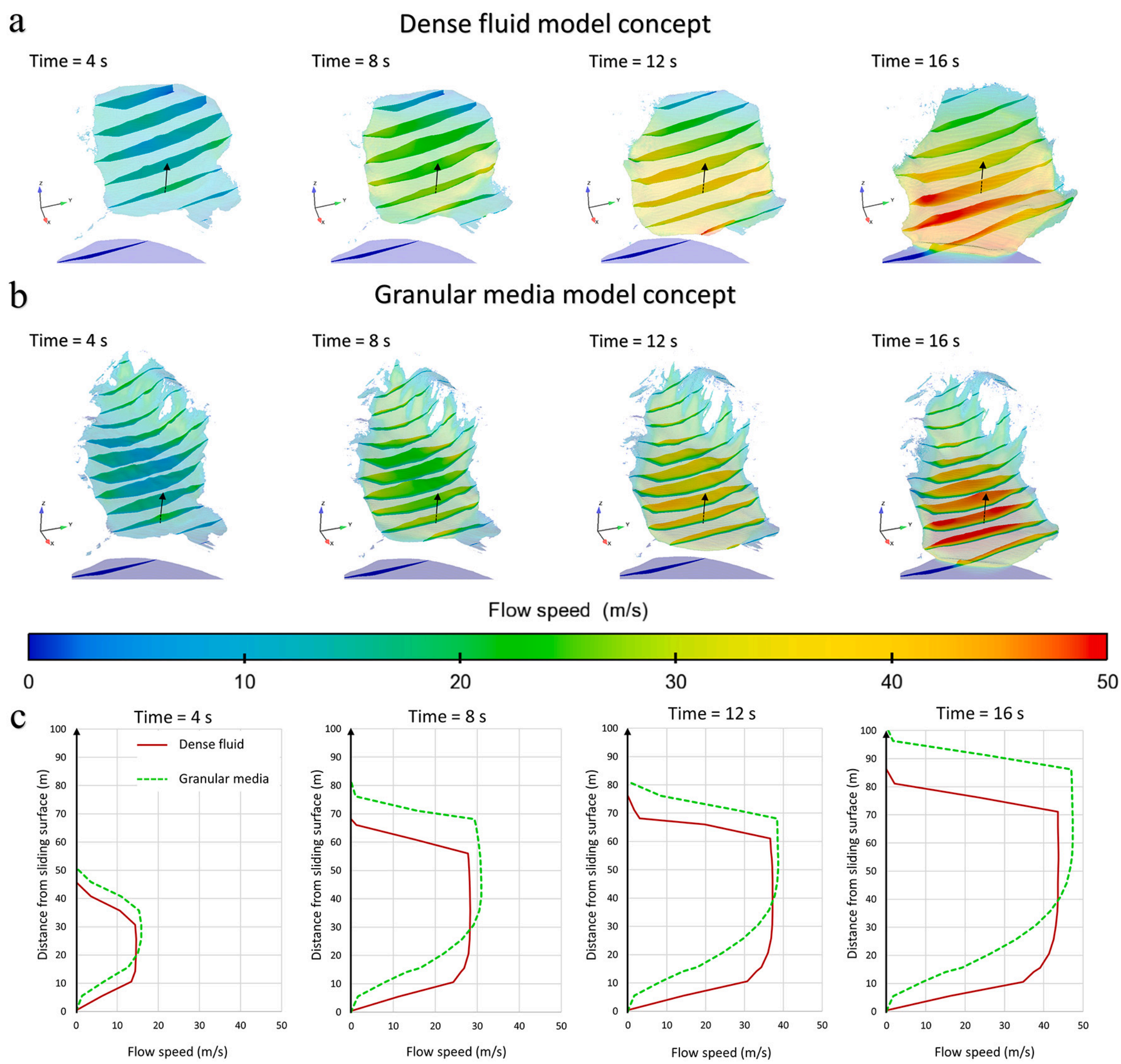

Fig. 8. Flow speed distribution of the sliding mass in motion along vertical cross-sections, for an example of a) the dense fluid model (volume of 26 Mm^3 with ρ_f of 2350 kgm^{-3} and sliding surface R_r 1 m), and of b) the granular media model (volume of 49.4 Mm^3, with a ρ_g of 2350 kgm^{-3}, a ρ_{mx} of 2220 kgm^{-3}, and φ_g of 40°). c) Through a line probe (black arrow in a, b) perpendicular to the sliding surface, it is possible to observe the increasing flow speed distribution in time, along the vertical direction, for the dense fluid model (red full line) and the granular media model (dashed green line). (For interpretation of the references to colour in this figure legend, the reader is referred to the web version of this article.)

entered the water body while 24 Mm^3 of the G.M. mass has already entered (value close to the estimated volume that triggered the tsunami, 26 Mm^3). Since the numerical code is not able to reproduce the physics of the sliding mass, for both model concepts the entire volume flows into the fiord, and the remaining debris in the scar area is not recreated. Despite this, the wave does not appear to be affected by the remaining volume still entering the water body, as most of the energy is almost immediately transferred after the slide impact (Mulligan and Take, 2017).

Similar trends, given the two model concepts, are observed for both impacting flow momentums (in B_1, Fig. 9e), where a maximum flow momentum is estimated equal to 1.39e[11] $kgms^{-1}$ (rapidly increasing from 12 to 19 s) for the D.F. and 1.46e[11] $kgms^{-1}$ (increasing from 13 to 24 s) for the G.M. (Table 4). Considering the cumulative distribution, the D.F. has more momentum compared to the G.M. (until 27 s). Despite the different volumes adopted for the two model concepts, more momentum is initially transferred to the water by the D.F., occurring faster and more impulse-like than by the G.M. This is confirmed by observing the resulting wave momentum (Fig. 9e), where at the baffle B_2 values of 1.23e[11] and 1.13e[11] $kgms^{-1}$ are computed for the wave resulting from the D.F. and the G.M. respectively. The momentum transferred from the impacting mass to the water is about 77.4–88.5% of the impacting momentum resulting for the G.M. and the D.F. respectively. Considering further locations at $B_{2–3}$ and B_3 (see values in Table 4), a linear relation describes wave momentum dissipation in the impact area (equation in Fig. 9e), where a difference of about 69–74% from B_2 to B_3 is estimated.

5.2. Inundation in the impact area (near-field analysis)

This *sec*tion focuses on the resulting wave run-up at the Hoof Hill Fan (Fig. 10) as a consequence of the impulse wave generated with the two model-concepts, for different set-up (section 4) and input parameters (section 3.3).

The inundation process given by the D.F. is reproduced considering an R_r of the sliding surface equal to 1 m which gives a reliable impact intensity. The R_r of the topographic surface has a strong effect on the run-up height (Fig. 10a), especially for areas featuring a low slope inclination. For a ρ_f of 2350 kgm^{-3}, the recreated run-up for higher topographic R_r values is closest to the observed one. The run-up height is often overestimated, particularly at further locations from the coastline

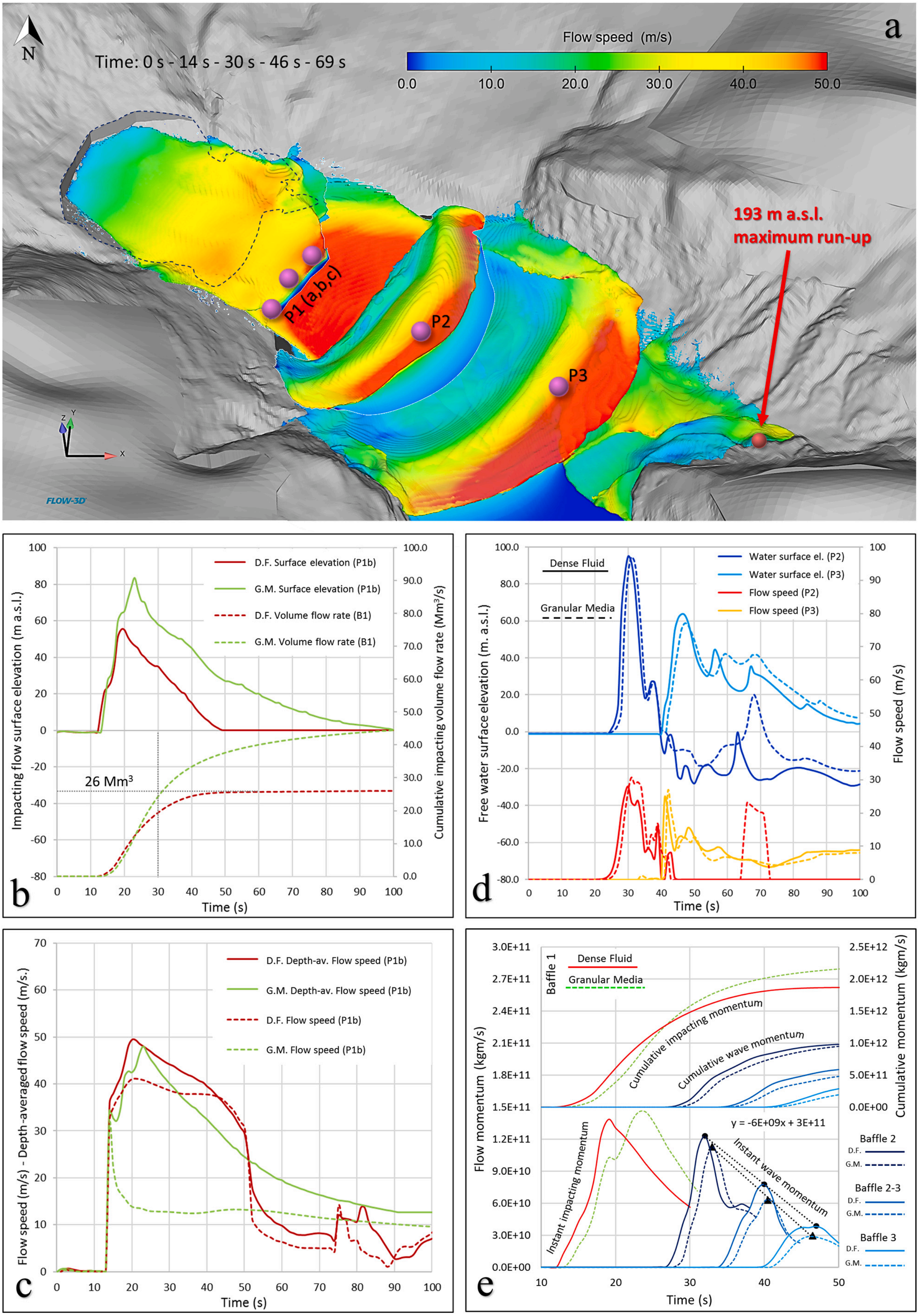

(caption on next page)

Fig. 9. a) Overview of the wave dynamics (generation and inundation for the dense fluid model) in the impact area for the simulation times steps of 0-14-30-46-69 s (isosurfaces refer to the flow speed); for the specific position of the history probes (P) and flux surface (B) refer to Fig. 7a. The diagrams show the impact process and the wave characteristics for two simulations with the dense fluid model (D.F. with ρ_f of 2350 kgm^{-3} and sliding surface R_r 1 m) and the granular media model (G.M. with a ρ_g of 2350 kgm^{-3}, a ρ_{mx} of 2220 kgm^{-3}, and φ_g of 40°). b) Impacting flow surface elevation (full lines, recorded at the probe P1b) and cumulative impacting volume flow rate (dashed lines, obtained from the flux surface, Fig. 6) for the D.F. (in red) and the G.M. (in green). c) Flow speed (dashed line) and depth-averaged flow speed (full line) distribution in time (recorded at the probe P1b) for the D.F. (in red) and the G.M. (in green). d) Free water surface elevation and flow speed for the impulse wave at its maximum crest elevation (P2) and the coastline of the Hoof Hill Fan (P3) for the D.F. (full lines) and the G.M. (dashed lines). e) Impacting flow momentum in time for the D.F. (red full line) and the G.M. (green dashed line), wave momentum (full-line and dashed line given the D.F. and the G.M. respectively), and corresponding cumulative distribution obtained from the flux surfaces (baffles in Fig. 6). (For interpretation of the references to colour in this figure legend, the reader is referred to the web version of this article.)

Table 4
Values for the maximum impacting flow momentum and the maximum wave momentum (and corresponding cumulative value) given the different model concepts.

	Baffle 1		Baffle 2		Baffle 2–3		Baffle 3	
	Dense Fluid	Granular Media	D.F. Wave	G.M. Wave	D.F. Wave	G.M. Wave	D.F. Wave	G.M. Wave
Maximum Flow Momentum (kgm/s)	*1.39E+11*	*1.46E+11*	*1.23E+11*	*1.13E+11*	*7.77E+10*	*6.30E+10*	*3.84E+10*	*2.95E+10*
Cumulative Flow Momentum (kgm/s)	*4.81E+11*	*8.58E+11*	*3.46E+11*	*3.11E+11*	*2.90E+11*	*2.13E+11*	*2.00E+11*	*9.65E+10*
Time (s)	19.00	24.00	32.00	33.00	40.00	40.50	47.00	46.50

and at the maximum run-up site. At the maximum run-up, a decreasing flow depth of 9–5.5-4-3.5 m is estimated for increasing R_r of 1–2–3-4 m. There is also a reduction in the simulated flooded area at the Hoof Hill Fan (Fig. 10a), compared to the observed ones, decreasing from 24.1% to 9.3% difference with increasing R_r. On the contrary, minor changes are observed for the resulting run-up given different values of the ρ_f. Locally, a higher value of ρ_f results in higher run-up elevations and larger flooded areas (Fig. 10b) with a percentage difference from 9.9% to 13.1% with increasing ρ_f and increasing flow depth of 3.5-4-5 m at the maximum run-up.

Similarly, the run-up recreated with the G.M. is analyzed for several combinations of the ρ_g, thus different ρ_{mx} (equal to 95% of ρ_{cpvf}), and diverse φ_g (sec. 4.1 and Table 3). A value of 3 m for R_r for the topographic surface is adopted, as it appears (based on the results with the D. F.) to be well representative of the vegetated topographic conditions at the site.

Although there are no significant variations in the run-up height for different φ_g, minor but still quantifiable changes are given for different ρ_g values (and thus for the ρ_{mx}, Fig. 10c). Contrary to what is reported for the D.F., lower values of ρ_g contribute to higher run-ups, with a decreasing percentage difference of the flooded area from 13.2% to 6.5% for an increase of the ρ_g. In addition, a reduction in flow depth of 4–2.5-0 m at the maximum run-up site occurs.

Finally, a comparison of the two modeling approaches which approximate the field observations best is shown in Fig. 10d. This involves a D.F. with ρ_f of 2350 kgm^{-3}, a sliding surface roughness R_r of 1 m and a topographic surface roughness R_r of 3 m; and a G.M. with a ρ_g of 2350 kgm^{-3}, a ρ_{mx} of 2220 kgm^{-3}, φ_g of 40°, and a topographic surface roughness R_r of 3 m. Generally, it can be stated that the simulated run-up is recreated quite well, but overestimations are reported for both models (lower for the G.M.). These mainly occur along the channel at the upper end of the delta, where inundation is largely attributed to backflow flowing down from the southern slopes of the Hoof Hill Fan (light blue arrows in Fig. 10 d).

Fig. 11 shows a vertical projection of the run-up for the same examined cases. Close to the observed value of 136 m a.s.l. the run-up is recreated well, the models overestimate the run-up from distances of 1500 m to almost 3500 m. Some explanations might refer to the impact area since the numerical model is unable to recreate the disintegration of the glacier caused by the landslide failure, which might dissipate a portion of the energy at the impact location. Moreover, at the Hoof Hill Fan, the wave removes vegetation and erodes debris from the delta during the inundation phase, thereby increasing its density and viscosity. This may have slowed the inland wave flow, resulting in a lower observed run-up compared to the modeling results.

Additionally, some underestimations are observed for distance intervals of 0–500 m and 3500–4000 m, corresponding mostly to very steep slopes. This can be related to some numerical limitations in pre-processing the solid bodies with regards to the adopted cell size and in computing the flow dynamics along sub-vertical surfaces (as already observed in Franco et al., 2020), together with possible irregularities and simplifications of the reconstructed topographic surface in Flow3D.

5.3. *Wave propagation and inundation along the whole fiord (far-field analysis)*

The goal of the simulations is to recreate wave dynamics along the entire fiord, to analyze how the fiord geometry influences wave characteristics, to reproduce the inundation process and the run-up. Observation gauges for flow measurements (see Appendix B for the history data description) enable a better understanding of the wave propagation process (Fig. 12a) and observations of its attenuation from the source to the fiord's mouth (Fig. 13).

- T 30–90 s: the wave proceeds straight forward out of the impact area, where two following reflected waves are also observed (Fig. 12b), resulting from the first wave reflection on the cliffs south of Hoof Hill Fan and the slope north the Hoof Hill Fan.
- T 90–150 s: the wave proceeds at high speed through the upper basin, the deepest part of the fiord. The secondary reflected wave brings inundation of steep slopes from the fiord up to high elevations, especially on the east flank of the fiord, with maximum elevations of 110 m a.s.l. (113 m a.s.l. observed, Fig. 1b).
- T 150–210 s: the wave propagates forward and approaches the first peninsula, where the fiord orientation changes from an N-S into an N.E.-S.W. direction. A large area on the east flank of the fiord is flooded (Fig. 1, 12a).
- T 210–270 s: due to the presence of a hill on the peninsula, the wave splits into two fronts. After breaking on the coastline, one front inundates the large delta and runs up the hill on the north peninsula (Fig. 12a). The other front proceeds to open sea.
- T 270–330 s: the wave front flows upon the shallower part of the fiord. Several higher wave crest peaks follow, still included in the same whole wave body. At the same time, the northern side of the southern peninsula is completely flooded (Fig. 1, 12a).
- T 330–420 s: the tsunami propagates through the southern basin of the fiord.
- T 420–660 s: the wave disperses as it approaches the mouth of the Taan Fiord, evolving into a long period wave. At the end of the

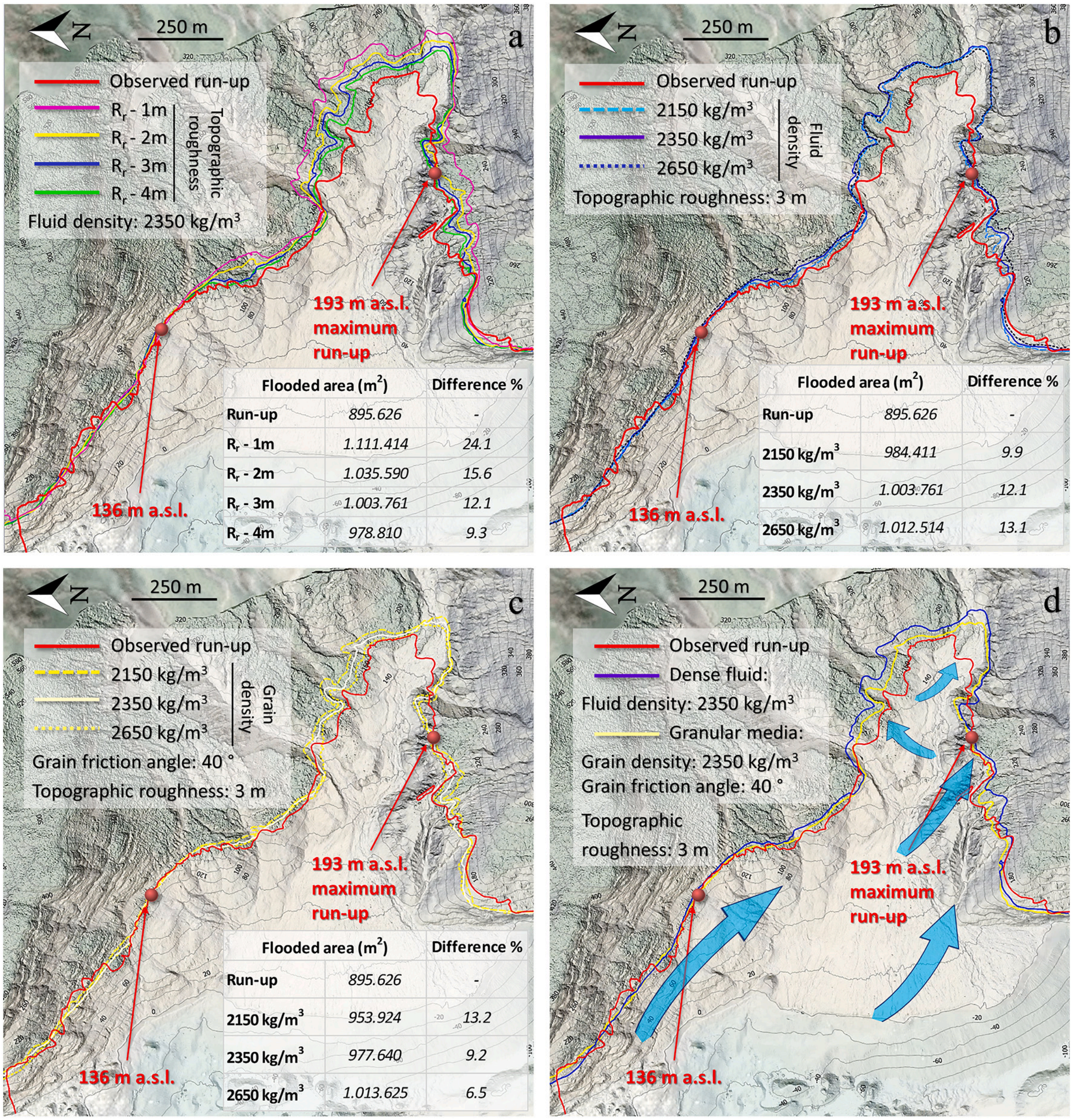

Fig. 10. Resulting run-up at the Hoof Hill Fan for different model settings and approaches compared to the observed run-up (red line). The tables show the differences in the area ($m^{2)}$ and percentage of the flooded areas for the observed and the recreated run-up. a) Run-up obtained for the D.F. with different values of R_r for the topographic surface (1-2-3-4 m) and equal R_r of 1 m for the sliding surface and fluid density ρ_f of 2350 kgm^{-3}. b) Run-up obtained for the D.F. and different values of ρ_f (2150-2350-2360 kgm^{-3}) and equal R_r of 1 m and 3 m for the sliding and topographic surface respectively. c) Run-up obtained for the G.M. and different values of grain density ρ_g (2150-2350-2360 kgm^{-3}), thus different values of mixture density ρ_{mx} (2032-2220-2502 kgm^{-3}, 95% of ρ_{cpvf}), and equal values of grain friction angle φ_g of 40° and topographic R_r of 3 m. d) Comparison of two examples (that best fit the observations) of the resulting run-up for the D.F. (blue line) and the G.M. (yellow line) with the observed one (red line). The blue arrows show the flow direction of the simulated wave during the inundation process. (For interpretation of the references to colour in this figure legend, the reader is referred to the web version of this article.)

simulation, the land next to the fiord mouth is flooded by the outcoming wave (pink area in Fig. 12a).

The induced wave by the landslide is the primary cause of inland flooding, but a significant contribution is made by the reflected waves generated in the impact area (Fig. 12b). For the given wave by the G.M. these are immediately involved in the main wave body (see P4 in Fig. 12a), thus influencing wave characteristics from the beginning of its propagation phase, and consequently increasing its elevation, speed, and energy while flowing along the fiord.

In Fig. 13, the propagation process and dispersion for the primary impulse wave generated from both model-concepts, expressed with the total hydraulic head, is illustrated. The reaction of the wave to changes in the fiord floor (so in water depth) and fiord shape is shown. The reported values represent the mean wave propagation speed (from 48 to 26 ms^{-1}). Generally, the wave produced by the G.M. has more energy compared to the D.F. induced wave, attributed to the higher surface elevation (eg. Fig. 12a) but also higher wave speed.

At the beginning of the propagation process, in the north part of the fiord (P2-P6), the mean propagation speed for the two models is the same. From the impact area to the upper north basin (P2-P4), an increased mean propagation speed of 48 ms^{-1} is estimated. Due to the significant energy dissipation in the impact area, a lower speed of 40 ms^{-1} between P4 and P5 (corresponding to the greatest depth of the fiord between −140 and − 160 m) is observed, then decreasing to 36 ms^{-1} (P5-P6). This further decrease can be related to the friction of the

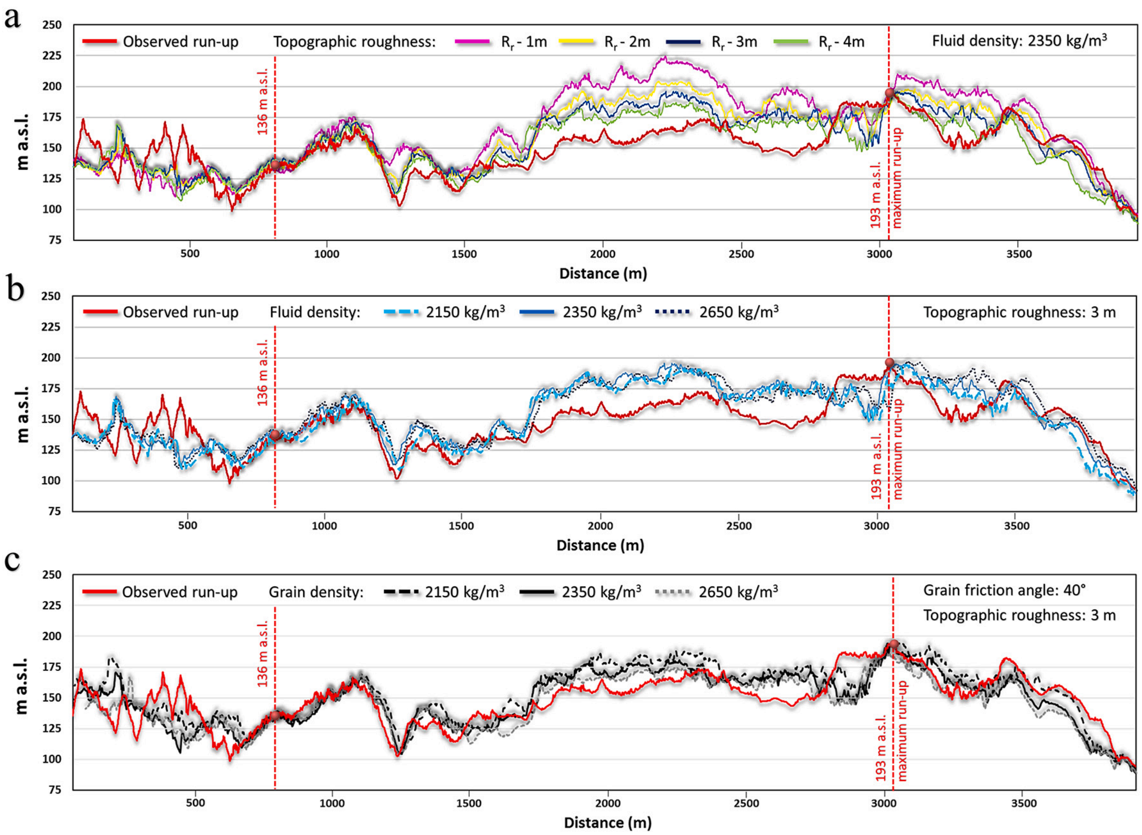

Fig. 11. For the same results presented in Fig. 10 a-b-c the run-up is shown on a vertical projection, where the distance of reference is the one of the observed run-up (red line). a) Run-up obtained for the D.F. with different values of R_r for the topographic surface (1-2-3-4 m) and equal R_r of 1 m for the sliding surface and fluid density ρ_f of 2350 kgm^{-3}. b) Run-up obtained for the D.F. and different values of ρ_f (2150-2350-2360 kgm^{-3}) and equal R_r of 1 m and 3 m for the sliding and topographic surface respectively. c) Run-up obtained for the G.M. and different values of grain density ρ_g (2150-2350-2360 kgm^{-3}), thus different values of mixture density ρ_{mx} (2032–2220-2502 kgm^{-3}, 95% of ρ_{cpvf}), and equal values of grain friction angle φ_g of 40° and topographic R_r of 3 m. (For interpretation of the references to colour in this figure legend, the reader is referred to the web version of this article.)

steep, narrow slopes of the fiord, and the constant shallowing of the fiord bottom from −160 to −100 m. From here onwards, the waves produced by the different models begin to behave differently (in Fig. 13 orange arrow and violet arrow for the G.M. and the D.F. respectively), especially as the first and second wave crests merge. Despite the significant decrease in water depth from −100 m to −60 m (P6-P7), the wave generated by the G.M. maintains a constant mean propagation speed of 36 ms^{-1}, while the wave from the D.F. decreases its mean speed to about 33 ms^{-1}. From P7 to P8 the fiord has a shallower water depth (about −50 m) and the waves flow with lower mean propagation speeds of 28 and 29 ms^{-1} (for the G.M. and the D.F. respectively). Further, in the southern basin, the water depths increase again (from −60 to −120 m), and the mean wave propagation speed is estimated to be about 29 ms^{-1} for both models. As the southern basin has a maximum water depth of about −130 m (P9-P10), the wave reaccelerates with a mean speed of 31–32 ms^{-1}. From P10 forward, influenced by fiord enlargement and additional decreases in water depth from −120 to −80 m (locally even to −40 m), the wave disperses with a decreasing mean propagation speed equal to about 26 ms^{-1} for both models. A final delay of 10 s in P11 for the D.F wave is observed, compared to the G.M. wave.

The wave attenuation phase takes place almost 16 km from the Taan fiord head to the seaside of the Icy Bay from 94 to 100 m to 6–8 m in wave amplitude. Reflected waves play a fundamental role in the flooding of steep slopes in the northern part of the fiord up to high elevations (P2-P6) merging into the first wave front, facilitating relatively high wave energy preservation up to the mouth of the fiord (P6-P11). This results in different behaviors of the waves generated by the two model concepts, where the wave from the D.F., having less energy involved in the propagation process, is more influenced by the changes in fiord geometry and water depth compared to the wave generated by the G.M. Moreover, this has consequences on the inland inundation process and the definition of the run-up.

Generally, some local underestimations of the run-up obtained with the D.F. are observed along with the entire domain, particularly on the eastern flanks of the northern part of the fiord and locally on the southern peninsula (Fig. 14a, blue line). In this last location, the wave did not recreate the observed run-up in its entirety, but it follows the trimline quite well.

With the D.F. the important influence of the topographic R_r on the run-up definition and the inundation process far away from the slide source is also demonstrated. A simple example is shown at the peninsula's location (Fig. 14c), where a lower topographic R_r leads to a higher run-up and vice versa. On the contrary, the R_r does not influence wave characteristics in open water.

In contrast, the run-up computed with the G.M. approximate the observed one well (Fig. 14a, light yellow line), with some local overestimations mostly in the center area of the fiord, especially at the northern slope on the hill and locally at the inner side of the southern peninsula. Additionally, for different values of grain density (and mixture density), the run-up is mostly recreated accurately, where some local differences are observed on land (Fig. 14.d) but no significant effects on wave characteristics in open water are noticed.

It is also noted that some local run-ups are not the product of the first main wave but are defined by some back-reflected flows as e.g. at the western side of the small hill on the northern peninsula (T about 340 s) and also at the western side of the southern peninsula (T about 460 s)

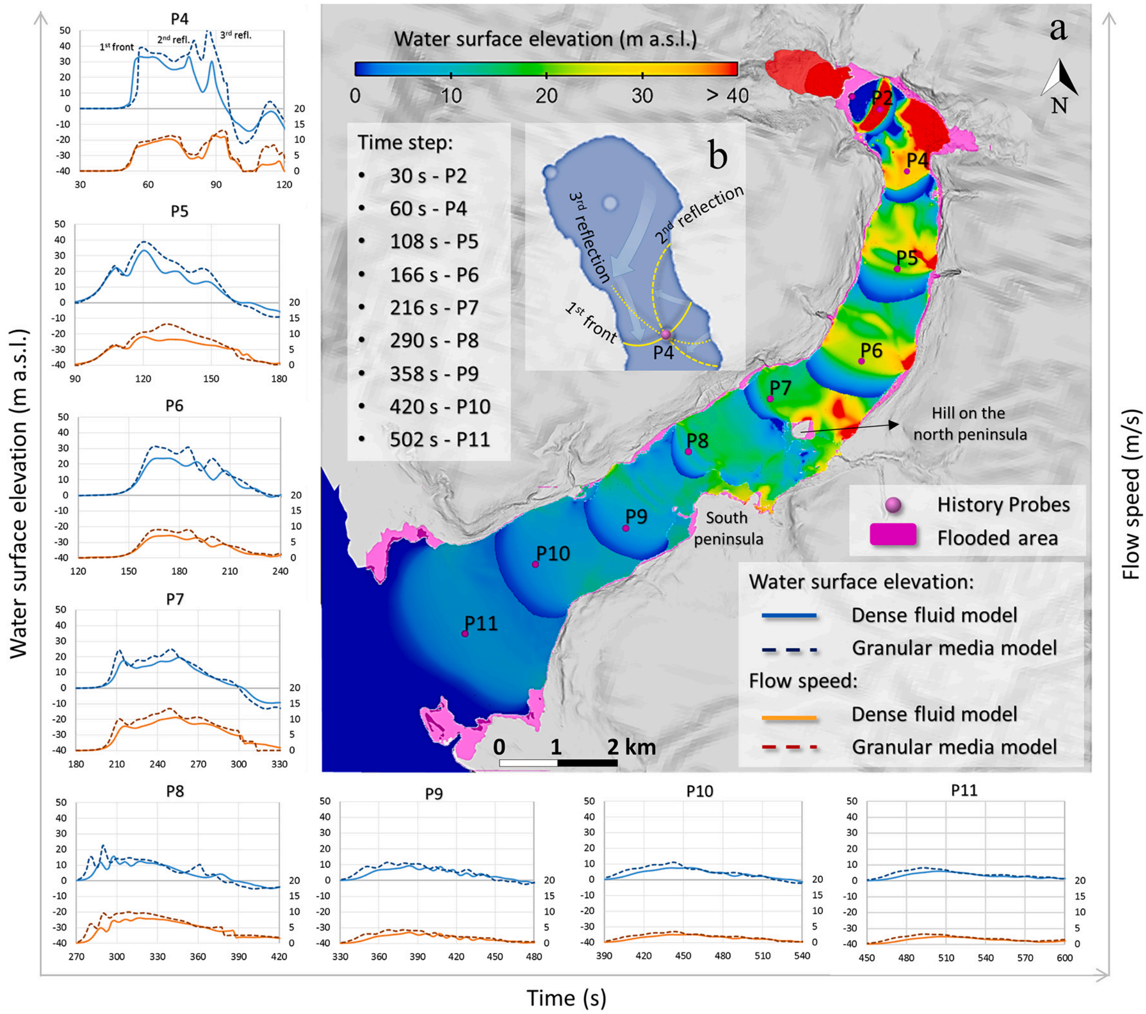

Fig. 12. a) Wave dynamics for the whole fiord domain (at different time steps from T 30–502 s) and diagrams showing the wave characteristics for the dense fluid model (full line, ρ_f of 2350 kgm^{-3} and sliding surface R_r 1 m) and the granular media model (dashed line, with a ρ_g of 2350 kgm^{-3}, a ρ_{mx} of 2267 kgm^{-3} 97% of ρ_{cpvf}, and φ_g of 40°) at its passage through the probes P2-P11 (the isosurfaces show the water surface elevation above sea level). b) Scheme showing the position of the first wavefront at P4 and the further second and third reflected waves.

(blue arrows in Fig. 14 c, d). Observing the flow speed vectors computed during the simulations at these locations, it appears that they are very close to the flow direction identified by the tsunami deposition records in the field (Higman et al., 2019), which implies that the models reproduce the wave flow dynamics of the Taan Fiord event quite realistically.

6. Discussion

6.1. Applicability and limits of the applied numerical models

Numerical models allow for the replication of natural phenomena with certain simplifications related to the equations implemented in the code, the used numerical methods, and the availability of the required data. In addition to appropriately choosing the modeling approach and set-up, the performance of a numerical model depends greatly on the reliability of input data. Concerning modeling a L.I.T. like the Taan Fiord 2015 event, if the intention is to simulate the sliding body as the wave initiation trigger, the definition of an adequate impact volume is one of the most important inputs for the model set-up. Constraining this volume by field measurements and a comprehensive event reconstruction increases the accuracy of the model results. Regarding the different approaches for the numerical simulations in this work, the D.F. represents a very simplified method to recreate the impact intensity, where only the impacting volume is utilized to generate the wave. The G.M., which is implemented as a high concentration continuum for the Taan Fiord case study, forms a more sophisticated method to model a sliding mass impacting a water body. Here, the geotechnical input gives the possibility to better qualitatively replicate the physical phenomena. Still, the granular media model as implemented in Flow3D is not a process-conform modeling approach for a granular flow (where the solid particles and the fluid must be treated individually and their interactions computed), but a simplification referring to a single-phase, continuous, incompressible fluid. An appropriate application can be achieved by employing a multi-phase model which considers the different materials and rheological behaviors in the mixture, the interactions between particles and fluid and computes the corresponding velocities together with the dynamical evolution of the mixture density (in eg. Pudasaini and Mergili, 2019), and where also the submerged mass transport can be reproduced to observe further consequences.

Utilizing the D.F. concept, the same implemented models are activated for the whole simulation time to recreate the wave dynamics (Fig. 7). Using the G.M. concept, the turbulence-viscosity model must be deactivated during the impact phase and the first stage of the wave formation, to then be reactivated (with a restart-option) to simulate further wave dynamics. It is additionally recommended not to deactivate the G.M. after the restart (in the near field analysis, Fig. 7) since its deactivation would lead to computing the remaining portion of the

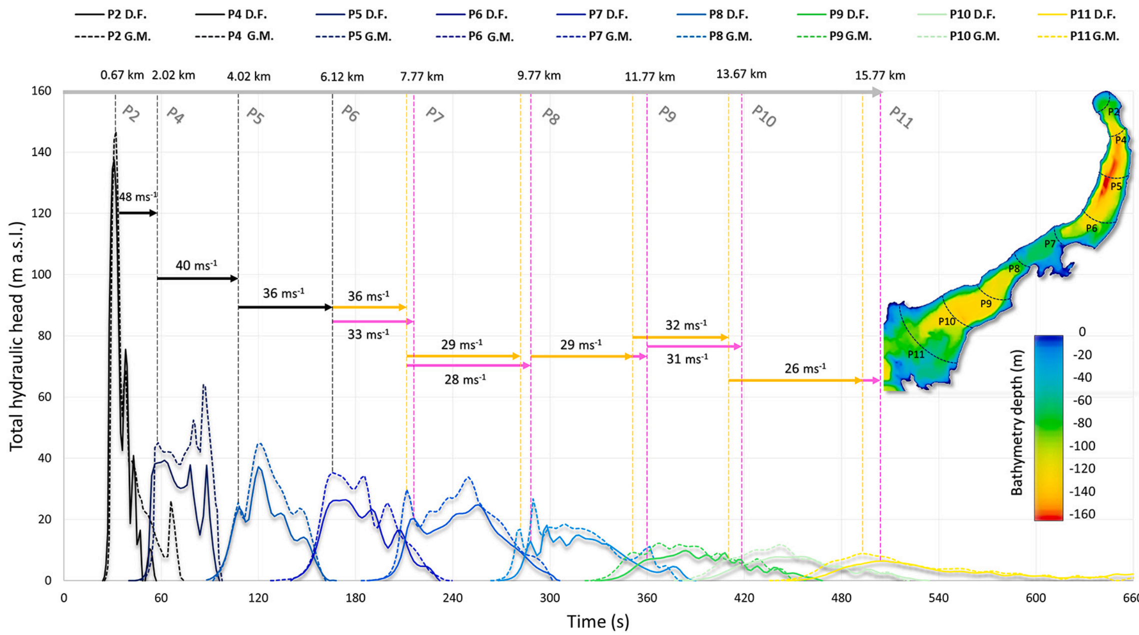

Fig. 13. For the same examples presented in Fig. 12, the wave attenuation process during its propagation along the fiord is expressed with the total hydraulic head. The full and dashed lines represent the generated waves based on the dense fluid and the granular media models respectively. Despite differences in the total hydraulic head, the waves generated by the different approaches flow with the same mean propagation speed until P6 (black arrows), changing afterwards (referring to the orange arrow and violet arrow for the G.M. and the D.F. respectively). (For interpretation of the references to colour in this figure legend, the reader is referred to the web version of this article.)

subaerial sliding volume as a fluid. This implies that, by the end of the simulations, this volume would enter the water body as a second impulse trigger with high speed, thus falsifying the outputs for the wave dynamics.

Moreover, it has been observed that the still-active G.M. does not affect calculations for the wave propagation and inundation, since the further generated wave is computed with the turbulence-viscosity model. To increase the computation performance (and decrease the output file size) for the far-field analysis, it is suggested to deactivate the G.M. (and the mesh block of the impact area) once the wave is propagating far from the slide source.

Despite the differences in the two applied modeling approaches, the combination of the investigated factors (see section 5.1) gives a resulting impulse wave that is quite similar for both concepts, although slightly higher for the G.M. Minor differences in wave characteristics can be related to the adopted "slide source" model at the impact stage and the 3D topographic effect while the wave is generating and further propagating. The 3D effect also explains the differences in results, given the different input data, whenever these appear not directly correlated. Moreover, in the far-field analysis, more energy involved in the wave propagation process is noticed for the G.M. approach.

6.2. Implications for wave hazard assessment and mapping

An additional objective of this study is to evaluate the applicability of the adopted modeling approaches (D.F. and G.M.) as potential methods for the forward analysis and evaluation of wave hazards. In this work the two models successfully reproduced the tsunami event 2015 at the Taan Fiord, thus demonstrating their efficient application, but some notes are additionally reported.

Regarding the application of the specific modeling approaches, the dense fluid model is simple to understand and therefore easy to set up, where only one input parameter (ρ_f) is required. If the numerical model is well-conceived, the computation time can be short (in this study ranging between 10 and 18 h), allowing the possibility to run several different scenarios. Despite this, the dense fluid is not a model that can be easily applied to various types of landslides, but mostly to those that act like fluids, meaning that an assumption of the bulk slide volume must be made. Relevant support can be provided by a landslide run-out analysis to check the applicability of this model and its set-up, but wherever this is not feasible, a detailed understanding of the physics regarding the landslide collapse phase (and possibly its rheology) is necessary. Concerning the 2015 Taan Fiord event, substantial knowledge and data are available and the new findings (section 3) lead to the hypothesis of a rotational landslide, where the D.F. is adoptable and only the impacting volume (observed on-site) is used to generate the wave.

In comparison, the G.M. requires a set-up linked to geotechnical inputs, so that its implementation can cover more possibilities for landslide reproduction where the material can be assumed as debris. This allows for the possibility to utilize the total estimated slide volume at the site, without any additional assumptions which are often required for the D.F. However, the model application is more complex, where a certain amount of user experience is recommended and a proper understanding of the role of the various input parameters, implemented in the code is needed. Indeed, many parameters are required for the set-up, which implies the necessity of a proper database, possibly based on direct observations. Otherwise, the analysis must be carried empirically where intervals of parameters are given (in eg. the φ_g and ρ_g in this study). Generally, the configuration of the G.M. is not as simple as the D.F. because the process that is designed to be simulated drives the selection of the input parameters and model settings (which can strongly vary from case to case). Specifically, for an analysis of a L.I.T., a restart-option is required to further implement turbulence models for wave reproduction, meaning that at least two simulations per scenario are carried out. Furthermore, slower computational times (from 2 up to 26 h per simulation) are needed due to the complexity of the model itself. This may be a disadvantage for sensitivity studies, or when many scenarios need to be simulated in the context of forwarding hazard analysis. A deterministic analysis of a few preselected, realistic scenarios would be beneficial when applying this modeling concept.

Apart from the pros and cons of the proposed modeling approaches, a general overestimation of the flooded area is observed in the near field

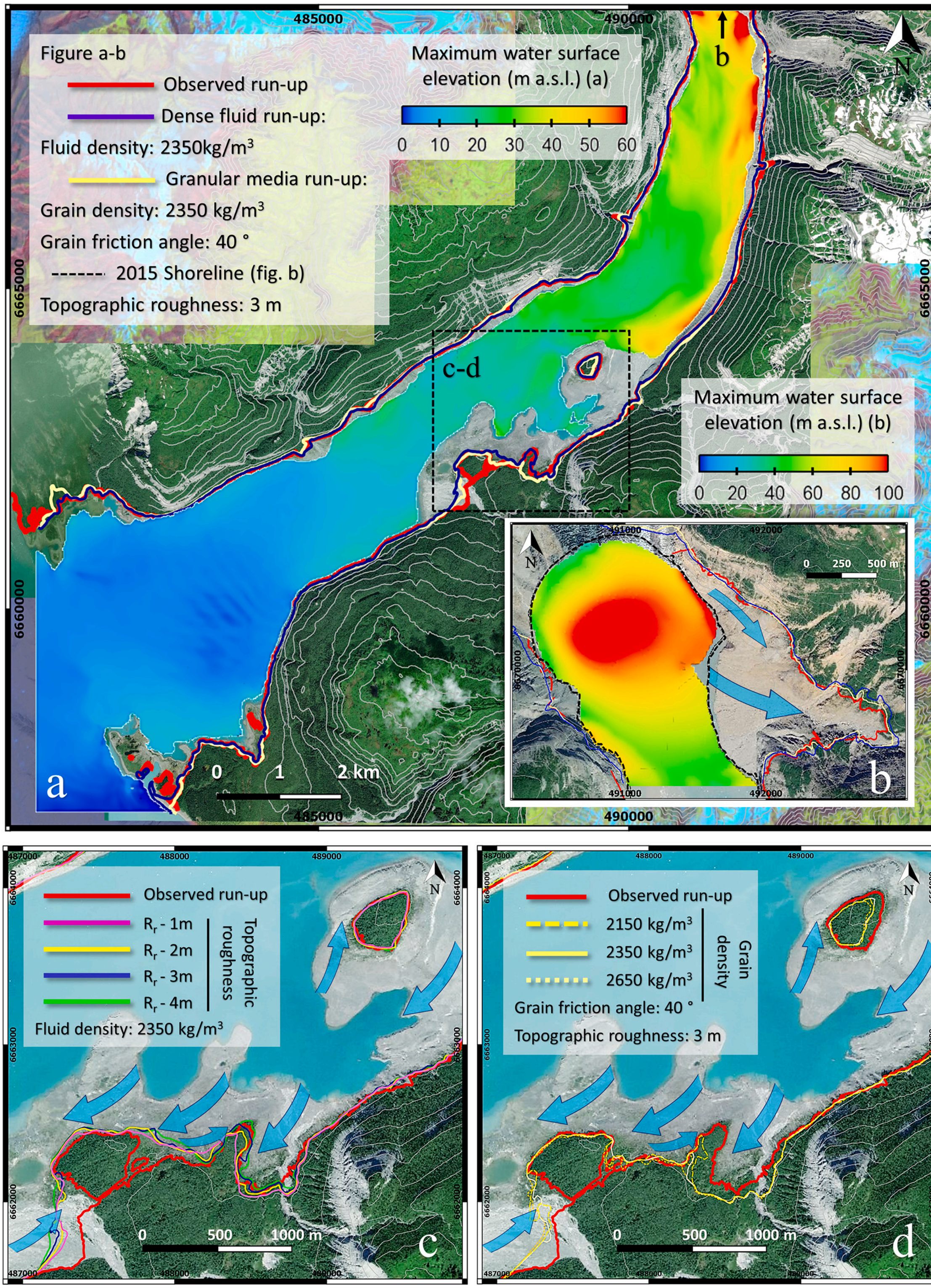

Fig. 14. Comparison of the resulting inundated area and related run-up, for the dense fluid model (blue line) and the granular media model (yellow line) for a) the whole bay and b) for the impact area. The isosurfaces show the maximum water surface elevation a.s.l. recorded in open water overall the simulation with the granular media model. Run-up at the peninsulas at the centre of the bay obtained for c) the D.F. with different values of R_r for the topographic surface (1-2-3-4 m) and equal fluid density ρ_f of 2350 kgm^{-3} and d) for the G.M. with different values of grain density ρ_g (2150-2350-2360 kgm^{-3}), thus different values of mixture density ρ_{mx} (2075-2267-2555 kgm^{-3}, 97% of ρ_{cpvf}), and equal values of grain friction angle φ_g of 40° and topographic R_r of 3 m. The light blue arrows show the wave flow direction, as observed from the simulations, during the inundation process. Background source: USGS LandsatLook (Landlook Viewer) - Esri, DigitalGlobe, GeoEye, Earthstar Geographics, CNES/Airbus DS, USDA, USGS, AeroGRID, IGN, and the GIS User Community, last access 10/06/2020. (For interpretation of the references to colour in this figure legend, the reader is referred to the web version of this article.)

analysis of the Taan Fiord case study, indicating that both models are on the conservative side for hazard assessment in the areas next to the slide source. On the contrary, some underestimations in flooding are noticed in the far-field analysis for the D.F. Better reproduction of the run-up in the far-field (locally overestimating to the observed one) is given for the simulations with the G.M., proving that this is likely on the safe side for hazard evaluation far away from the slide source.

In hydraulic hazard assessment, the standard final product is a collection of maps considering different scenarios (each related to a probability of occurrence, Li et al., 2021) or approaches, where the information on flow characteristics is presented as relative isosurfaces, typically the maximum flow depth, maximum flow speed and the flow intensity as the maximum value resulting from the product between the flow depth and the depth-averaged speed (for all computed time steps in a simulation). Maps showing isosurfaces of the above-mentioned variables (Figs. 15, 16) are presented as a useful application for wave hazard assessment in this study. Notably, it appears that the trend of the resulting intensity contours at the near field are similar to those of the maximum flow depths (Fig. 15), suggesting that the latter has a significant role in the potential hazard estimation in areas close to the slide source. In the far-field, contours obtained from the simulations with the G.M. generally show higher flow depths compared to the results with the D.F. approach (Fig. 16 a,b).

It must be considered when investigating transient flow, that every

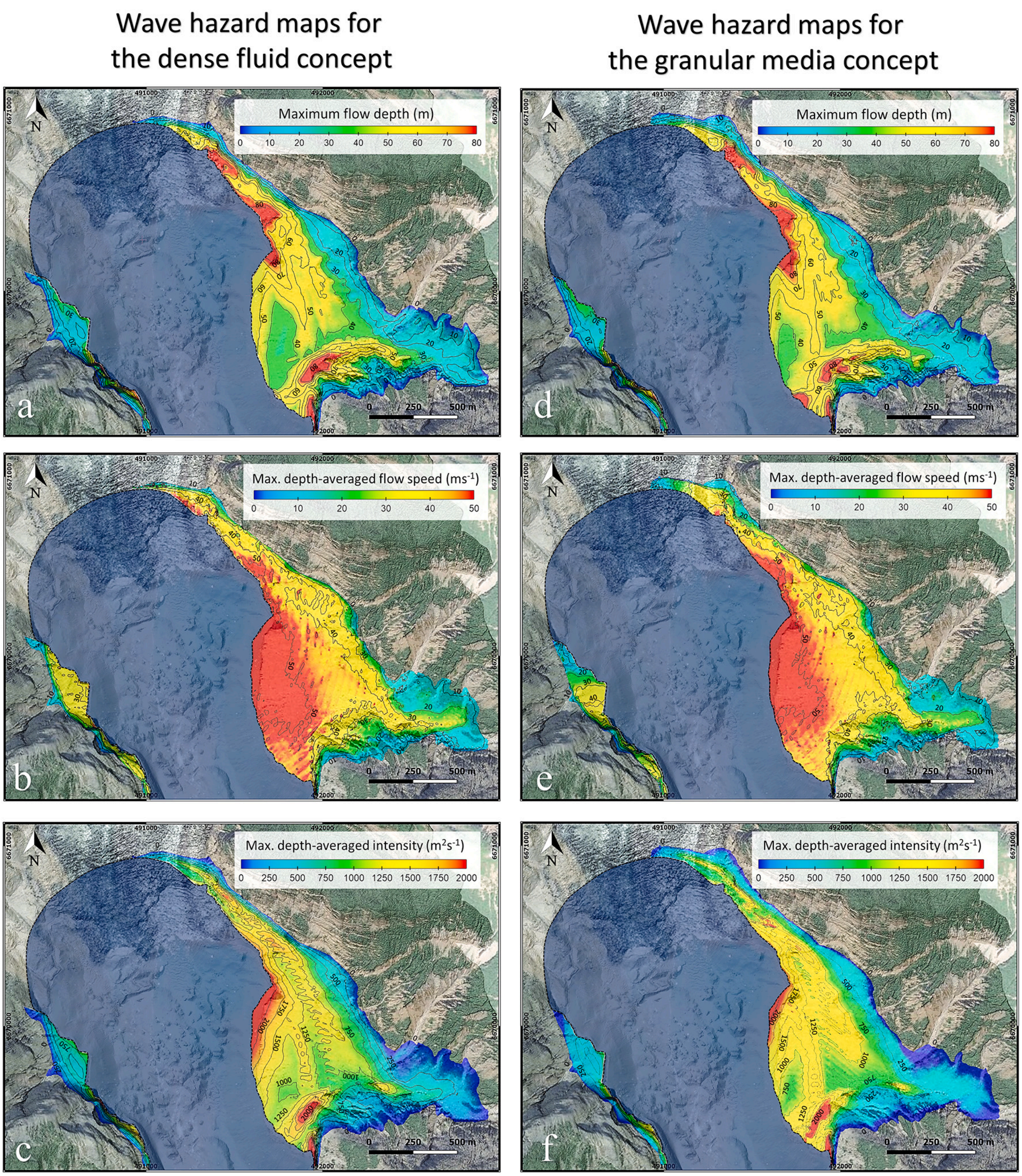

Fig. 15. Wave hazard maps, at the impact area, for an example of a,b,c) the dense fluid model (ρ_f of 2350 kgm^{-3} and R_r equal to 1 m and 3 m for the sliding and topographic surfaces respectively), and d,e,f) the granular media model (ρ_g of 2350 kgm^{-3} and a ρ_{mx} of 2220 kgm^{-3}, φ_g of 40° and R_r equal to 3 m for the topographic surface). The isosurfaces show a,d) the maximum flow depth (m), b,e) the maximum depth-averaged flow speed (ms^{-1}), and c,f) the maximum depth-averaged intensity (m^{2}s^{-1}). Background source: bathymetric and topographic surface from Haeussler et al., 2018; USGS LandsatLook (Landlook Viewer) - Esri, DigitalGlobe, GeoEye, Earthstar Geographics, CNES/Airbus DS, USDA, USGS, AeroGRID, IGN, and the GIS User Community, last access 10/06/2020.

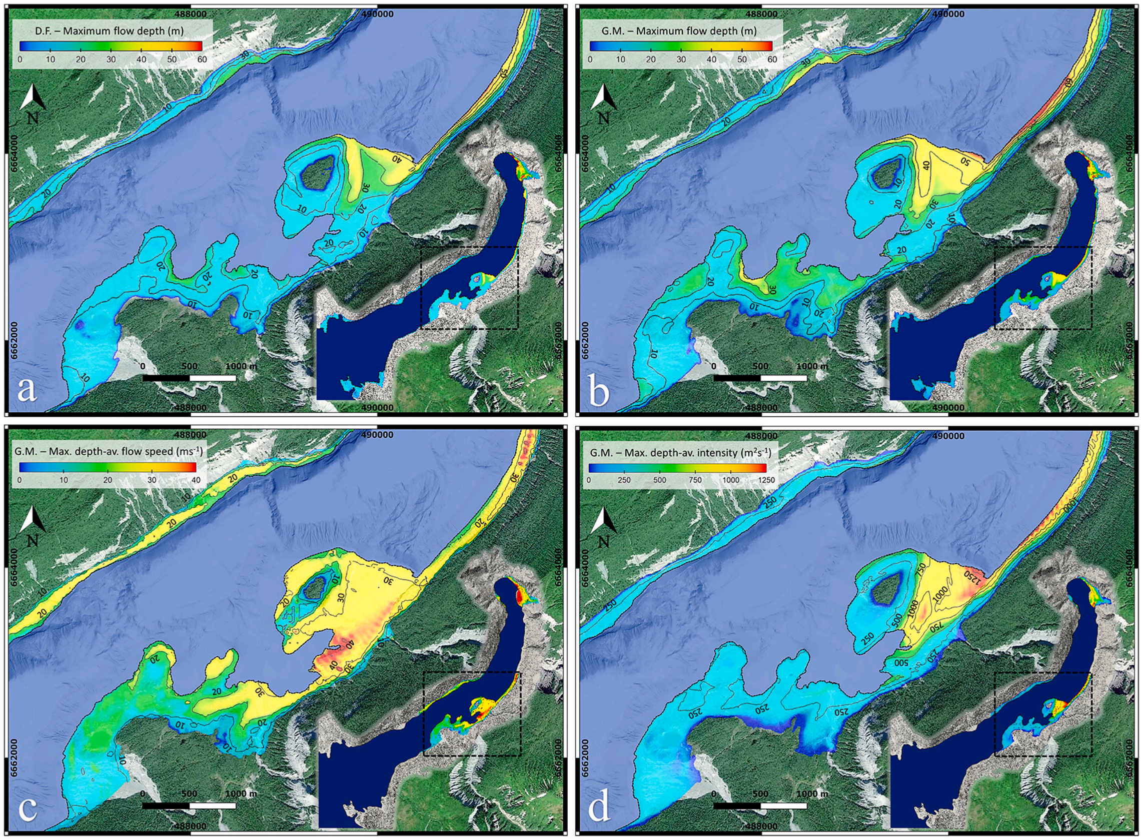

Fig. 16. For the same example presented in Fig. 14a (see legend), the wave hazard maps, resulting from the wave inundation at the center location of the Taan Fiord, illustrate the isosurfaces for the maximum flow depth (m) given a) the dense fluid model and b) the granular media model. The wave hazard maps for c) the maximum depth-averaged flow speed (ms^{-1}) and d) the maximum depth-averaged intensity (m^{2}s^{-1}), are shown for the granular media model. Background source: bathymetric and topographic surface from Haeussler et al., 2018; USGS LandsatLook (Landlook Viewer) - Esri, DigitalGlobe, GeoEye, Earthstar Geographics, CNES/Airbus DS, USDA, USGS, AeroGRID, IGN, and the GIS User Community, last access 10/06/2020.

computational time step must be checked to obtain the real maximum value of a variable. While this is the case for the maximum flow depth in Flow3D, meaning that this is checked at every time step and it is available wherever there has been water at any time in the domain, the maximum depth-averaged flow speed and maximum intensity have to be post-processed in FlowSight (with the Calculator ToolBox). This implies that these variables are evaluated at each "data time step" that has been specified by the user in the model set-up, meaning there is no guarantee in obtaining the real maximum by the selected time step. A possible solution is to increase the selected data interval (decreasing the time step), but it must be considered that this would largely increase the output file size, with the risk of obtaining an "un-processible" file. It is on the user to identify a data time step that gives a reasonable ratio of data accuracy and file size, depending on the modeling purposes. For this study, a data time step of 1 s and 2 s have been selected for near and far-field analysis respectively (with an output file size ranging from 30 GB up to 70 GB per simulation). Given the large dimension of the model domain and the reproduced physical hazard processes, these time steps provide a good approximation for the required variables and are thus useful for further wave hazard mapping.

6.3. Further potential research

The presented geomorphological analysis together with thoroughly researching available literature allowed for the definition of a proper database (Table 3) with the main governing parameters useful for further hydrodynamic numerical analyses, but it is encouraged to also perform a detailed slope-stability analysis, to assess landslide dynamics and links between landslide and glacier dynamics. Limitations are mostly represented by the availability and quality of multi-temporal data like DEMs, where an even higher temporal resolution of the available data would be required to compensate for missing seasonal information (especially concerning the glacier dynamics).

The subjective interpretation of the landslide dynamics (section 3.2) reasonably combines all the information to describe the entire complex process, justifying the significant vertical displacement (Fig. 3c) that occurred only after the year 2012. This could be explained by the assumed semi-rigid rotation of the sliding body and the consequent formation of the listric faults as described in stage (2). It may also be assumed that the listric faults could have already formed in the first stage of the slope destabilization (stage 1), where the antithetic discontinuities represent only secondary features of the landslide, and the large displacements after 2012 could have occurred due to the weakening of the mechanical properties of the slope material concerning glacier movements. A stress-strain analysis and a proper run-out analysis, adopting representative rheology of the landslide, might provide better insight into the landslide failure process, the influence of the glacier or a possible underground water table, and evaluate the proposed model concept for the tsunamigenic landslide. Geotechnical investigation and tests on the slide material would help to verify the reliability of the proposed dataset to be applied to further research on the Taan Fiord 2015 case study, which would help in clarifying which mechanism caused the slow-moving landslide body to accelerate and catastrophically fail.

Since this is the first work in which the granular media model, implemented in Flow3D, is used to recreate a L.I.T. event in a natural basin, further research in other cases would be required to evaluate the results presented and the modeling procedure adopted. Still, a comparison with other process-conform models in recreating the physical landslide process (and in initiating the impulse wave) at the Taan Fiord, like a multi-phase model or a particles model (eg. the S.P.H.), where rheological models can be also considered, might be valuable for the reliability of the proposed modeling concept.

7. Summary and conclusions

The tsunami event of October 2015 in Taan Fiord presents an ideal well-constrained case study where the application of different models in Flow3D is possible to initiate the impulse wave. In this way, this case study also allows generic methodology development and testing of its applicability for cascading hydraulic hazard evaluation, eventually to be of great use for further application in other settings beyond the here studied at the Taan Fiord. In particular, the availability of multi-temporal pre-and post-event datasets (DEMs from 2000 to 2016) allows an analysis of the landslide body before the final collapse. Insights into the deformation process, an update of the displaced volumes, and a complete interpretation of the landslide dynamics at the Taan Fiord are provided. Information and new data carried out from the geomorphological analysis are fundamental in implementing further hydrodynamics simulations. The applied models not only cover all involved processes but also cover a physically and correct, highly detailed, and complex representation of wave dynamics and run-up in a large area of interest. The main novelty is the adoption of the granular media model, in Flow3D, to recreate a L.I.T. event, which allows a good reproduction of the subaerial impact process and the resulting impulse wave utilizing just one code. As a final product resulting from the application of 3D hydrodynamic models, hazard maps showing the isosurfaces with regards to the maximum flow depths, the flow speed, and the intensities are presented (Fig. 15-16). This hazard mapping approach represents a valuable tool for potential wave hazard assessment in mountain basins, but it can be also applied to assess other hydraulic hazards.

The main findings regarding the geomorphological analysis are following listed:

- A significant vertical displacement on the slope has been observed between 2012 and 2014 (about −90 m) where a negative change in volume (about −28.5 Mm^3) is recognizable in the landslide area and a positive change on the glacier (Table 2). The latter can be attributed to bulging from the landslide toe to the glacier, possibly related to the action of listric faults within the landslide body.
- The final landslide collapse in 2015 is estimated with a volume of 49.4 Mm^3, resulting from the raster difference between the Arctic DEM AK V.2–2014 and the DEM 2016 of Haeussler et al. (2018). Of this amount, 26 Mm^3 entered the fiord and possibly triggered the tsunami.

The method adopted to study the landslide dynamics in this work (using open-source software like QGIS) represents a suitable and straightforward approach to qualitatively and quantitatively study a moving landslide body, where a detailed spatiotemporal analysis provides fundamental insights and new outcomes. Based on the results from the accomplished geomorphological analyses, a model concept for the landslide is defined in a way so that the adoption of both the dense fluid (D.F.) and the granular media (G.M.) models are successfully applied using the Flow3D software. To gain a better understanding of the applicability of the proposed modeling approaches, the outputs obtained from the different models are thus compared:

- the choice of the defined impact volumes for the different model concepts (26 Mm^3 for the D.F. and 49.4 Mm^3 for the G.M.) each resulting in a successful reproduction of the generated wave (with a maximum wave crest ranging between 93 and 101 m);
- the flow speed of the sliding mass evolves faster for the D.F. than for the G.M., where a general computed impact speed distribution varies from 32 ms^{-1} up to 49.5 ms^{-1} (comparable with the empirically estimated 36–45 ms^{-1});
- the momentum of the impacting flow plays a key role in inducing the impulse wave (Fig. 9e), where 77.4–88.5% is transferred to the water, faster and more impulse-like for the D.F., and more distributed for the G.M.;
- in the near field analysis, an overestimation (9–12%) of the observed run-up is obtained with both approaches, where the maximum run-up of 193 m a.s.l. is recreated with a varying flow depth of 0–9 m;
- the propagation models show how the first wavefront and immediately reflected secondary waves are responsible for the entire inundation process and the consequently flooded areas at the Taan Fiord;
- the topographic surface roughness plays a crucial role for the inundation process and the run-up, where a roughness value of 3 m gives a good approximation of the observed run-up, meaning that this is representative for the vegetation height and small geomorphological features on the headland;

Finally, for both models, despite the different properties, a comparable impulse wave is obtained with similar characteristics (Fig. 9d) to those reported in the literature (section 1), meaning that both approaches are adequate in reproducing the impulse wave at the Taan Fiord, considering the detailed parameter database.

It is further concluded that the best-fitting results to the observations are obtained with mean values of the input parameters (D.F.: ρ_f of 2350 kgm^{-3} and R_r equal to 1 m and 3 m for the sliding and topographic surfaces respectively; G.M.: ρ_g of 2350 kgm^{-3}, φ_g of 40° and R_r equal to 3 m for the topographic surface).

Furthermore, considering the discussed advantages and limitations (section 6), the applicability of these modeling approaches for efficient wave hazard assessment in mountain water basins is demonstrated. It can be concluded in this context that:

- the dense fluid modeling approach is easy to use and low time consuming, where fast outputs are produced, but its applicability in triggering the impulse wave needs to be evaluated;
- the granular media better reproduces gravitational mass movement processes, but is more time-consuming, it requires more input parameters and a more complex model set-up; a deterministic analysis of few realistic scenarios would still represent a useful application for assessing the potential wave hazard.

Data availability

Supplementary data comprising of:

- model codes
- the reconstructed bathymetry and topography as STL-file
- the bathymetric map on October 2015 and related shapefile (contour lines)
- data table regarding the solid-fluid mixture density
- table summarizing the diverse model approaches available in Flow3D

that support the findings of this study are available on the following directory:

https://doi.org/10.5281/zenodo.5011681

The simulation video is available on the following links:

https://www.youtube.com/watch?v=zxyYlMvzSbM&t=95s

Computational resource and hardware components

- Processor: Intel® Core™ i7–3820 CPU 3.60 GHz;
- RAM: 32 GB;
- System type: 64-bit Operating System;

- Graphics card: GeForce GTX 6602 (Integrated RAMDAC, total available memory 4096 MB);
- Number of core license tokens checked out: 8 (Flow3D parallel license code).

Authors' contributions

AF designed the case study and the main research goals, with support from JM and MS for the landslide process interpretation, from BG for the modeling in Flow3D and BSM for the granular media model-concept set-up. AF prepared the manuscript, tables and figures with contributions from JM, BSM, MS and BG. All authors discussed, reviewed and edited the different versions of the manuscript.

Declaration of Competing Interest

The authors declare that they have no conflict of interest.

Acknowledgements

This study is funded by the University of Innsbruck in support of the doctoral program "Natural Hazards in Mountain Regions". It is related to the project "Wave formation, propagation and run-up in natural mountain lakes from a cascade hazard perspective – analysis and modeling of triggering processes, lake's morpho-dynamics and potential downstream hazard effects". Thank is owed to the Journal Editor and the (anonymous) reviewers, whose comments and remarks greatly improved the quality of this paper. A great thank is further owned to Andreas Huber (the University of Innsbruck, Unit of Hydraulic Engineering) for the support to efficient DEMs co-registration, to Markus Grünzner and Robert Feurich (Flow Science Germany) for the quick support in problem-solving, to Harold Alvarez (Flow Science Latin America, Colombia) for the great support in the granular media model understanding and functionality. Thanks to Thèo St. Pierre Ostrander for revising the English syntax of the manuscript. Further thank goes to Mario Crevato (Limes – Arheologija prostora/Archaeology for the territory) for the preliminary informatics and geomorphological elaborations support for the landslide analysis.

Appendix A. History probes data for the impact process and wave generation

One example of both model-concepts is considered each: i) D.F.: ρ_f of 2350 kgm^{-3} and sliding surface R_r of 1 m; ii) G.M.: ρ_g of 2350 kgm^{-3}, ρ_{mx} of 2220 kgm^{-3} and φ_g of 40°.

- T 0–16 s: during the sliding process, the flow speed (in terms of velocity magnitude) evolves differently for the two models (Fig. 8 a, b): the D.F. presents a more uniform speed (Fig. 8a) along the vertical compared to the more distributed speed in the G.M. (Fig. 8b). At a line probe, located in the lower part of the sliding mass and set perpendicular to the sliding surface (black arrow in Fig. 8), the flow speed distribution is analyzed. In the D.F. flow speed increases from 14 to 44 ms^{-1} within 12 s (T 4–16 s), where lower values occur in the first 10 m above the sliding surface. In the G.M. flow speed increases from 16 to 47 ms^{-1} with a variable distribution along the vertical up to 50 m above the sliding surface. This variability could be due to the shear strength effect acting inside the granular media mass, and where friction has a major influence on the flow speed closer to the sliding surface.
- T 16–25 s: impacting the sea, for the D.F. and the G.M. a maximum elevation of 55 m a.s.l. and 84 m a.s.l. is recorded in P1b at 20 and 23 s, respectively (Fig. 9 b), which suggests that a larger volume of water is remobilized by the G.M. after the impact, due to a comparatively higher slide front height. At the probes P1a-b-c, a flow speed ranging from 32.5 to 43.5 ms^{-1} and a depth-averaged flow speed from 36.5 to 49.5 ms^{-1} is observed during the impact process for the D.F. (Fig. 9 c). In the G.M. the impacting flow speed results in a lower value of about 38 ms^{-1} due to the position of the probes closer to the topographic surface. In contrast, the depth-averaged speed ranges between 35 and 48 ms^{-1} and it is comparable with the results from the D.F.
- T 25–35 s: the wave reaches values of 94 m a.s.l. and 95 m a.s.l. recorded in P2 for the D.F. and the G.M. respectively. Additionally, a flow speed of about 30–33 ms^{-1} is observed.
- T 35–50 s: the wave reaches the opposite coastline at about 34 s from the impact (T 46–48 s), with a wave crest elevation of about 63 and 58.5 m a.s.l. (and a flow speed of 24–26 ms^{-1}) resulting from the D.F. and the G.M., respectively (data recorded in P3, Fig. 9 a, d).
- T 50–75 s: the maximum run-up of 193 m a.s.l. is reached about 55 and 57 s from the impact (T 69–72 s, Fig. 9 a).

A.1. History probes data for the wave propagation and inundation process

For the D.F. a fluid density of 2350 kgm^{-3} and an R_r equal to 1 m for the sliding surface is adopted. For the G.M. a grain friction angle of 40° and an R_r for the topographic surface equal to 3 m are chosen. Additionally, a slight change in the mixture density ρ_{mx} is required, with values of 2075–2267-2555 kgm^{-3} equal to the 97% of ρ_{cpvf} (see table in data availability) to achieve the same impact intensity as recreated in the near field analysis since a coarser mesh is used (see section 4.2). The same examples considered in section 5.1 are proposed for the description of the propagation process (Fig. 12a), where data mainly refer to the first wavefront at the gauges.

- T 30–90 s: a resulting wave crest elevation of 33 and 39 m a.s.l. for the D.F. and the G.M. respectively, and a flow speed of 11 ms^{-1} in P4 is observed. Between 80 and 90 s, the second reflected wavefront which passes P4 has a crest elevation of 34 and 43 m a.s.l. (T 76 and 80 s) for the D.F. and the G.M. respectively. The third front has a crest elevation of 30 m a.s.l. (T 88 s) for the D.F., while for the G.M. the wave crest elevation is about 50 m a.s.l. (T 86 s). The latter is the result of the interference between the second reflection flowing backwards to the impact area and the third one moving forward, resulting in a much higher elevation compared to the crest height of the first wave. The D.F. does not show this wave interference.
- T 90–150 s: a wave elevation of 22 and 24 m a.s.l. for the D.F. and the G.M. respectively and a flow speed of 6.5 ms^{-1} are recorded in P5. It is noticed that a higher crest peak following the first one (T 120 s), results in 33 and 38.5 m a.s.l., thereby featuring also higher flow speeds of 10 and 13 ms^{-1} for the D.F. and the G.M. respectively.
- T 150–210 s: in P6 the above-described wave elevation crests merge in one whole wavefront, with a crest elevation of 24 and 31 m a.s.l and flow speeds of 7 and 9 ms^{-1} for the D.F. and the G.M. respectively.
- T 210–270 s: the wave brakes on the coastline with a surface elevation of about 40–50 m a.s.l and a flow speed of about 35 ms^{-1}. Flow depths on the inland vary between 10 and 30 m. In P7 a wave crest elevation of 17 and 24.5 m a.s.l. and flow speeds of 8 and 10 ms^{-1} are recorded for the D.F. and the G.M. respectively. This is followed by a second wave crest peak of 19 and 24 m a.s.l. at T 252–256 s.
- T 270–330 s: in P8 a wave crest elevation of 12 m a.s.l. (T 288 s) and 15 m a.s.l. (T 281 s), with a flow speed of 5–6 ms^{-1}, are observed for the D.F. and the G.M. respectively. Secondary wave crest peaks occur with an increase of the flow speed to about 8–10 ms^{-1}. At the northern side of the south peninsula flow depths of about 10–30 m and flow speeds between 5 and 15 ms^{-1} are observed.
- T 330–420 s: in P9 the wave body features several crests peaks with a maximum wave elevation of 8 and 11 m a.s.l. (and a flow speed of 4 ms^{-1}) for the D.F. and the G.M. respectively.

- T 420–660 s: the wave results in a period of about 136–140 s flowing over the P10 (T 388–524 s), where a maximum wave crest elevation of 7.5 and 11 m a.s.l. (and a flow speed of 3.5 ms^{-1}) are recorded for the D.F. and the G.M. respectively. Further in P11, a maximum wave crest elevation of 6 and 8 m a.s.l. together with a flow speed of 3 ms^{-1} are observed for the D.F. and the G.M. respectively.

References

Alvarez, H., Wendelbo, J., 2018. Estudio de 3 modelos matematico para simular olas producidas por derrumbes en embales yesfuerzos en compuertras (E. U. Flow Science Latin America, Colombia. Flow Science Inc. (ed.)). XXVIII Congresso latino-americano de hidraulica Buenos aries, Argentina, Septiembre de 2018.

Bagnold, R.A., 1941. The Physics of Blown Sand and Desert Dunes. William Morrow Co., New York.

Bartelt, P., McArdell, B., Graf, C., Christen, M., Buser, O., 2016. Dispersive pressure, boundary jerk and configurational changes in debris flows. Int. J. Eros. Control Eng. 9 (1), 1–6. https://doi.org/10.13101/ijece.9.1.

Basu, D., Green, S., Das, K., Janetzke, R., 2009. Numerical simulation of Surface Waves Generated by a Subaerial Landslide at Lituya Bay, Alaska. In: Proc. OMAE 2009, 28th Int. Conf. Ocean. Offshore Arct. Eng. May 31–June 5, 2009, Honolulu, Hawaii, pp. 1–14. https://doi.org/10.1115/1.4001442.

Bilal, M., Xing, A., Zhuang, Y., Zhang, Y., Jin, K., Zhu, Y., Leng, Y., 2021. Coupled 3D numerical model for a landslide-induced impulse water wave: a case study of the Fuquan landslide. Eng. Geol. 290 (May), 106209. https://doi.org/10.1016/j.enggeo.2021.106209.

Bloom, C.K., MacInnes, B., Higman, B., Shugar, D.H., Venditti, J.G., Richmond, B., Bilderback, E.L., 2020. Catastrophic Landscape Modification from a Massive Landslide Tsunami in Taan Fiord (Alaska).

Bregoli, F., 2015. Tsunamis Provoked by Fast Granular Landslides: 3D Laboratory Experiments on Generation and Initial Propagation of Waves. In Doctoral thesis. Universitat Politècnica de Catalunya.

Cannon, C.M., 2017. Data to support modeling of the 2015 Tyndall Glacier landslide, Alaska: U.S. Geological Survey data release. https://doi.org/10.5066/F73R0RR3.

Chung, T.J., 2010. Computational Fluid Dynamics. Cambridge university press.

Coe, J.A., Bessette-Kirton, E.K., Geertsema, M., 2018. Increasing rock-avalanche size and mobility in Glacier Bay National Park and Preserve, Alaska detected from 1984 to 2016 Landsat imagery. Landslides 15 (3), 393–407. https://doi.org/10.1007/s10346-017-0879-7.

Dai, C., Higman, B., Lynett, P.J., Jacquemart, M., Howat, I.M., Liljedahl, A.K., Dufresne, A., Freymueller, J.T., Geertsema, M., Ward Jones, M., Haeussler, P.J., 2020. Detection and assessment of a large and potentially-tsunamigenic periglacial landslide in Barry arm, Alaska. Geophys. Res. Lett. 1–9 https://doi.org/10.1029/2020gl089800.

Das, K., Janetzke, R., Basu, D., Green, S., Stamatakos, J., 2009. Numerical simulations of tsunami wave generation by submarine and aerial landslides using RANS and SPH models. Proc. Int. Conf. Offshore Mech. Arct. Eng. - OMAE 5, 581–594. https://doi.org/10.1115/OMAE2009-79596.

Deline, P., Hewitt, K., Reznichenko, N., Shugar, D., 2015. Rock avalanches onto glaciers. In: Landslide hazards, risks and disasters. Elsevier, pp. 263–319. https://doi.org/10.1016/b978-0-12-396452-6.00009-4.

Donev, A., Cisse, I., Sachs, D., Variano, E.A., Stillinger, F.H., Connelly, R., Torquato, S., Chaikin, P.M., 2004. Improving the density of Jammed Disordered Packings Using Ellipsoids. Science (80) 303 (5660), 990–993. https://doi.org/10.1126/science.1093010.

Du, J., Yin, K., Glade, T., Woldai, T., Chai, B., Xiao, L., Wang, Y., 2020. Probabilistic hazard analysis of impulse waves generated by multiple subaerial landslides and its application to Wu Gorge in three Gorges Reservoir, China. Eng. Geol. 276 (July), 105773. https://doi.org/10.1016/j.enggeo.2020.105773.

Duc, D.M., Khang, D.Q., Ngoc, D.M., Quynh, D.T., Thuy, D.T., Giang, N.K.H., Van Tien, P., Ha, N.H., 2020. Analysis and modeling of a landslide-induced tsunami-like wave across the Truong river in Quang Nam province, Vietnam. Landslides 17 (May), 2329–2341. https://doi.org/10.1007/s10346-020-01434-2.

Dufresne, A., Geertsema, M., Shugar, D.H., Koppes, M., Higman, B., Haeussler, P.J., Stark, C., Venditti, J.G., Bonno, D., Larsen, C., Gulick, S.P.S., McCall, N., Walton, M., Loso, M.G., Willis, M.J., 2018. Sedimentology and geomorphology of a large tsunamigenic landslide, Taan Fiord, Alaska. Sediment. Geol. 364, 302–318. https://doi.org/10.1016/j.sedgeo.2017.10.004.

Ersoy, H., Karahan, M., Gelişli, K., Akgün, A., Anılan, T., Sünnetci, M.O., Yahşi, B.K., 2019. Modelling of the landslide-induced impulse waves in the Artvin Dam reservoir by empirical approach and 3D numerical simulation. Eng. Geol. 249 (April 2018), 112–128. https://doi.org/10.1016/j.enggeo.2018.12.025.

Flow Science Inc., 2020. FLOW-3D®Solver, Version 12.2. Santa Fe, NM: Flow Science, Inc.

Franci, A., Cremonesi, M., Perego, U., Crosta, G., Oñate, E., 2020. 3D simulation of Vajont disaster. Part 1: numerical formulation and validation. Eng. Geol. 279 (around 2000) https://doi.org/10.1016/j.enggeo.2020.105854.

Franco, A., Moernaut, J., Schneider-Muntau, B., Strasser, M., Gems, B., 2020. The 1958 Lituya Bay tsunami – pre-event bathymetry reconstruction and 3D numerical modelling utilising the computational fluid dynamics software Flow-3D. Nat. Hazards Earth Syst. Sci. 20, 2255–2279. https://doi.org/10.5194/nhess-20-2255-2020.

Fritz, Hermann M., Hager, W.H., Minor, H.E., 2001. Lituya Bay case: rockslide impact and wave run-up. Sci. Tsunami Hazards 29 (1), 3–23.

Gabl, R., Seibl, J., Gems, B., Aufleger, M., 2015. 3-D numerical approach to simulate the overtopping volume caused by an impulse wave comparable to avalanche impact in a reservoir. Nat. Hazards Earth Syst. Sci. 15 (12), 2617–2630. https://doi.org/10.5194/nhess-15-2617-2015.

Gauthier, D., Anderson, S.A., Fritz, H.M., Giachetti, T., 2018. Karrat Fjord (Greenland) tsunamigenic landslide of 17 June 2017: initial 3D observations. Landslides 15 (2), 327–332. https://doi.org/10.1007/s10346-017-0926-4.

George, D.L., Iverson, R.M., Cannon, C.M., 2017. New methodology for computing tsunami generation by subaerial landslides: Application to the 2015 Tyndall Glacier landslide, Alaska. Geophys. Res. Lett. 44 (14), 7276–7284. https://doi.org/10.1002/2017GL074341.

Gonzalez-Vida, J.M., Macias, J., Jesus Castro, M., Sanchez-Linares, C., De La Asuncion, M., Ortega-Acosta, S., Arcas, D., 2019. The Lituya Bay landslide-generated mega-tsunami - Numerical simulation and sensitivity analysis. Nat. Hazards Earth Syst. Sci. 19 (2), 369–388. https://doi.org/10.5194/nhess-19-369-2019.

Gruber, S., Haeberli, W., 2007. Permafrost in steep bedrock slopes and its temperature-related destabilization following climate change. J. Geophys. Res. Earth Surf. 112, 10. https://doi.org/10.1029/2006JF000547.

Gualtieri, L., Ekström, G., 2018. Broad-band seismic analysis and modeling of the 2015 Taan Fjord, Alaska landslide using Instaseis. Geophys. J. Int. 213 (3), 1912–1923. https://doi.org/10.1093/GJI/GGY086.

Hackett, S.W., 1976. Regional Gravity survey of Beluga Basin and Adjacent Area. Cook Inlet Region, South-Central Alaska, Alaska Open-file Report 100, 41.

Haeussler, P.J., Gulick, S.P.S., McCall, N., Walton, M., Reece, R., Larsen, C., Shugar, D.H., Geertsema, M., Venditti, J.G., Labay, K., 2018. Submarine Deposition of a Subaerial Landslide in Taan Fiord. J. Geophys. Res. Earth Surf. 123 (10), 2443–2463. https://doi.org/10.1029/2018JF004608.

Haque, U., da Silva, P.F., Devoli, G., Pilz, J., Zhao, B., Khaloua, A., Wilopo, W., Andersen, P., Lu, P., Lee, J., Yamamoto, T., Keellings, D., Jian-Hong, W., Glass, G.E., 2019. The human cost of global warming: Deadly landslides and their triggers (1995–2014). Sci. Total Environ. 682, 673–684. https://doi.org/10.1016/j.scitotenv.2019.03.415.

Haritashya, U.K., Kargel, J.S., Shugar, D.H., Leonard, G.J., Strattman, K., Watson, C.S., Shean, D., Harrison, S., Mandli, K.T., Regmi, D., 2018. Evolution and controls of large glacial lakes in the Nepal Himalaya. Remote Sens. 10 (5), 798.

Harlow, F.H., Welch, J.E., 1965. A domain decomposition method for incompressible viscous flow of fluid with free surface. Phys. Fluids 8, 2182–2189. https://doi.org/10.1063/1.1761178.

Harlow, Francis Harvey, Nakayama, P.I., 1968. Transport of Turbulence Energy Decay Rate. Los Alamos Scientific Lab., N. Mex.

Harrison, S., Kargel, J.S., Huggel, C., Reynolds, J., Shugar, D.H., Betts, R.A., Emmer, A., Glasser, N., Haritashya, U.K., Klimeš, J., Reinhardt, L., Schaub, Y., Wiltshire, A., Regmi, D., Vilímek, V., 2018. Climate change and the global pattern of moraine-dammed glacial lake outburst floods. Cryosphere 12 (4), 1195–1209. https://doi.org/10.5194/tc-12-1195-2018.

Heller, V., 2009. Landslide generated impulse waves experimental results. Proc. Coast. Eng. Conf. 1313–1325.

Heller, V., Hager, W.H., 2010. Impulse product parameter in landslide generated impulse waves. J. Waterw. Port Coast. Ocean Eng. 136 (3), 145–155. https://doi.org/10.1061/(ASCE)WW.1943-5460.0000037.

Heller, V., Hager, W.H., Minor, H.-E., 2009. Mitteilungen 211 - Landslide Generated Impulse Waves in Reservoirs.

Higman, B., Shugar, D.H., Stark, C.P., Ekström, G., Koppes, M.N., Lynett, P., Dufresne, A., Haeussler, P.J., Geertsema, M., Gulick, S., Mattox, A., Venditti, J.G., Walton, M.A.L., McCall, N., Mckittrick, E., MacInnes, B., Bilderback, E.L., Tang, H., Willis, M.J., Loso, M., 2018. The 2015 landslide and tsunami in Taan Fiord, Alaska. Sci. Rep. 8 (1), 1–12. https://doi.org/10.1038/s41598-018-30475-w.

Higman, B., Geertsema, M., Shugar, D., Lynett, P., Dufresne, A., 2019. Alaska Park Science (Vol. 18, I, Issue August). National Park Service U.S. Department of the Interior, Alaska Region.

Hinze, J.O., 1975. Isotropic Turbulence. Turbul, Second Ed. McGraw-Hill, New York, pp. 165–204.

Hirt, C.W., 2010. A continuum model for high concentration granular media: Illustrated by application to sand core blowing. In: Flow Science Report 10-TN88.

Hirt, C.W., 2013. A FLOW-3D ® Continuum Model for Granular Media. Flow Science Report 02–13.

Hirt, C.W., Sicilian, J.M., 1985. A porosity technique for the definition of obstacles in rectangular cell meshes. In: Int. Conf. Numer. Sh. Hydrodyn. 4th.

Kafle, J., Kattel, P., Mergili, M., Fischer, J.T., Pudasaini, S.P., 2019. Dynamic response of submarine obstacles to two-phase landslide and tsunami impact on reservoirs. Acta Mech. 230 (9), 3143–3169. https://doi.org/10.1007/s00707-019-02457-0.

Karahan, M., Ersoy, H., Akgun, A., 2020. A 3D numerical simulation-based methodology for assessment of landslide-generated impulse waves: a case study of the Tersun Dam reservoir (NE Turkey). Landslides 17 (May), 2777–2794. https://doi.org/10.1007/s10346-020-01440-4.

Kim, G.B., Cheng, W., Sunny, R.C., Horrillo, J.J., McFall, B.C., Mohammed, F., Fritz, H.M., Beget, J., Kowalik, Z., 2020. Three Dimensional Landslide Generated Tsunamis: Numerical and Physical Model Comparisons. Landslides 17 (5), 1145–1161. https://doi.org/10.1007/s10346-019-01308-2.

Koppes, M., Hallet, B., 2006. Erosion rates during rapid deglaciation in Icy Bay, Alaska. J. Geophys. Res. Earth Surf. 111 (2), 1–11. https://doi.org/10.1029/2005JF000349.

Kos, A., Amann, F., Strozzi, T., Delaloye, R., von Ruette, J., Springman, S., 2016. Contemporary glacier retreat triggers a rapid landslide response, Great Aletsch Glacier, Switzerland. Geophys. Res. Lett. 43 (24), 12–466.

Li, Y., Chen, L., Yin, K., Zhang, Y., Gui, L., 2021. Quantitative risk analysis of the hazard chain triggered by a landslide and the generated tsunami in the Three Gorges Reservoir area. Landslides 18, 667–680. https://doi.org/10.1007/s10346-020-01516-1.

Mao, J., Zhao, L., Liu, X., Cheng, J., Avital, E., 2017. A three-phases model for the simulation of landslide-generated waves using the improved conservative level set method. Comput. Fluids 159 (October), 243–253. https://doi.org/10.1016/j.compfluid.2017.10.007.

Meigs, A., Sauber, J., 2000. Southern Alaska as an example of the long-term consequences of mountain building under the influence of glaciers. Quat. Sci. Rev. 19 (14–15), 1543–1562. https://doi.org/10.1016/S0277-3791(00)00077-9.

Meigs, A., Krugh, W.C., Davis, K., Bank, G, 2006. Ultra-rapid landscape response and sediment yield following glacier retreat, Icy Bay, southern Alaska. Geomorphology 78 (3–4), 207–221. https://doi.org/10.1016/j.geomorph.2006.01.029.

Mergili, M., Pudasaini, S.P., Emmer, A., Fischer, J.T., Cochachin, A., Frey, H., 2020. Reconstruction of the 1941 GLOF process chain at Lake Palcacocha (Cordillera Blanca, Peru). Hydrol. Earth Syst. Sci. 24 (1), 93–114. https://doi.org/10.5194/hess-24-93-2020.

Mih, W.C., 1999. High concentration granular shear flow. J. Hydraul. Res. 37 (2), 229–248.

Mulligan, R.P., Take, W.A., 2017. On the transfer of momentum from a granular landslide to a water wave. Coast. Eng. 125 (February), 16–22. https://doi.org/10.1016/j.coastaleng.2017.04.001.

Nichols, B.D., Hirt, C.W., Hotchkiss, R.S., 1981. Volume of fluid (VOF) method for the dynamics of free boundaries. J. Comput. Phys. 39 (1), 201–225.

Nie, Y., Pritchard, H.D., Liu, Q., Hennig, T., Wang, W., Wang, X., Liu, S., Nepal, S., Samyn, D., Hewitt, K., Chen, X., 2021. Glacial change and hydrological implications in the Himalaya and Karakoram. Nat. Rev. Earth Environ. 2 (2), 91–106. https://doi.org/10.1038/s43017-020-00124-w.

Nuth, C., Kääb, 2011. Co-registration and bias corrections of satellite elevation data sets for quantifying glacier thickness change. Cryosphere 5 (1), 271–290. https://doi.org/10.5194/tc-5-271-2011.

Paris, A., Okal, E.A., Guérin, C., Heinrich, P., Schindelé, F., Hébert, H., 2019. Numerical Modeling of the June 17, 2017 Landslide and Tsunami events in Karrat Fjord, West Greenland. Pure Appl. Geophys. 176 (7), 3035–3057. https://doi.org/10.1007/s00024-019-02123-5.

Pastor, M., Herreros, I., Fernández Merodo, J.A., Mira, P., Haddad, B., Quecedo, M., González, E., Alvarez-Cedrón, C., Drempetic, V., 2009. Modelling of fast catastrophic landslides and impulse waves induced by them in fjords, lakes and reservoirs. Eng. Geol. 109 (1–2), 124–134. https://doi.org/10.1016/j.enggeo.2008.10.006.

Pavlis, T.L., Chapman, J.B., Bruhn, R.L., Ridgway, K., Worthington, L.L., Gulick, S.P.S., Spotila, J., 2012. Structure of the actively deforming fold-thrust belt of the St. Elias orogen with implications for glacial exhumation and three-dimensional tectonic processes. Geosphere 8 (5), 991–1019. https://doi.org/10.1130/GES00753.1.

Pudasaini, S.P., Mergili, M., 2019. A Multi-phase Mass Flow Model. J. Geophys. Res. Earth Surf. 124 (12), 2920–2942. https://doi.org/10.1029/2019JF005204.

Rady, R., 2011. 2D-3D modeling of flow over sharp-crested weirs. J. Appl. Sci. Res. 7 (12), 2495–2505.

Roe, G.H., Baker, M.B., Herla, F., 2017. Centennial glacier retreat as categorical evidence of regional climate change. Nat. Geosci. 10 (2), 95–99.

Romano, A., Di Risio, M., Bellotti, G., Molfetta, M.G., Damiani, L., De Girolamo, P., 2016. Tsunamis generated by landslides at the coast of conical islands: experimental benchmark dataset for mathematical model validation. Landslides 13 (6), 1379–1393. https://doi.org/10.1007/s10346-016-0696-4.

Sassa, K., Dang, K., Yanagisawa, H., He, B., 2016. A new landslide-induced tsunami simulation model and its application to the 1792 Unzen-Mayuyama landslide-and-tsunami disaster. Landslides 13 (6), 1405–1419. https://doi.org/10.1007/s10346-016-0691-9.

Shean, D.E., Alexandrov, O., Moratto, Z.M., Smith, B.E., Joughin, I.R., Porter, C., Morin, P., 2016. An automated, open-source pipeline for mass production of digital elevation models (DEMs) from very-high-resolution commercial stereo satellite imagery. ISPRS J. Photogramm. Remote Sens. 116, 101–117. https://doi.org/10.1016/j.isprsjprs.2016.03.012.

Tan, H., Ruffini, G., Heller, V., Chen, S., 2018. A numerical landslide-tsunami hazard assessment technique applied on hypothetical scenarios at Es Vedrà, offshore Ibiza. J. Mar. Sci. Eng. 6 (4) https://doi.org/10.3390/jmse6040111.

Walder, J.S., Watts, P., Sorensen, O.E., Janssen, K., 2003. Tsunamis generated by subaerial mass flows. J. Geophys. Res. Solid Earth 108 (B5), 1–19. https://doi.org/10.1029/2001jb000707.

Wang, J., Ward, S.N., Xiao, L., 2015. Geophys. J. Int. 201 (1), 372–376. https://doi.org/10.1093/gji/ggv026.

Wang, J., Ward, S.N., Xiao, L., 2019. Tsunami Squares modeling of landslide generated impulsive waves and its application to the 1792 Unzen-Mayuyama mega-slide in Japan. Eng. Geol. 256 (February), 121–137. https://doi.org/10.1016/j.enggeo.2019.04.020.

Wang, J., Xiao, L., Ward, S.N., Du, J., 2021. Tsunami Squares modeling of the 2007 Dayantang landslide generated waves considering the effects in slide/water interactions. Eng. Geol. 284 (February), 106032. https://doi.org/10.1016/j.enggeo.2021.106032.

Ward, S.N., Day, S., 2010. The 1958 Lituya Bay landslide and tsunami a tsunami ball approach. J. Earthq. Tsunami 4 (4), 285–319. https://doi.org/10.1142/S1793431110000893.

Welch, J.E., Harlow, F.H., Shannon, J.P., Daly, B., 1968. The MAC method-a computing technique for solving viscous, incompressible, transient fluid-flow problems involving free surfaces. Los Alamos Sci. Lab. Rep. LA-3425 https://doi.org/10.1016/0021-9991(81)90145-5.

Williams, H.B., Koppes, M.N., 2019. A comparison of glacial and paraglacial denudation responses to rapid glacial retreat. Ann. Glaciol. 60 (80), 151–164. https://doi.org/10.1017/aog.2020.1.

Witt, K.J., 2017. Teil 1:Geotechnische Grundlagen. Grundbau-Taschenbuch (Part 1: Geotechnical basic, Foundation Engineering Pocketbook), , 8thXXVIII. Wiley, p. 988.

Wu, T.R., Vuong, T.H.N., Lin, C.W., Wang, C.Y., Chu, C.R., 2020. Modeling the slump-type landslide tsunamis part I: developing a three-dimensional bingham-type landslide model. Appl. Sci. 10 (18) https://doi.org/10.3390/APP10186501.

Xu, W.J., Yao, Z.G., Luo, Y.T., Dong, X.Y., 2020. Study on landslide-induced wave disasters using a 3D coupled SPH-DEM method. Bull. Eng. Geol. Environ. 79 (1), 467–483. https://doi.org/10.1007/s10064-019-01558-3.

Yakhot, V., Smith, L.M., 1992. The renormalization group, the ε-expansion and derivation of turbulence models. J. Sci. Comput. 7 (1), 35–61.

Zhang, Y., Li, D., Chen, L., Yin, K., Xiao, L., Fu, X., Glade, T., Leo, C., 2020. Numerical analysis of landslide-generated impulse waves affected by the reservoir geometry. Eng. Geol. 266 (June 2019), 105390. https://doi.org/10.1016/j.enggeo.2019.105390.

Zhao, T., Utili, S., Crosta, G.B., 2016. Rockslide and impulse wave modelling in the Vajont reservoir by DEM-CFD analyses. Rock Mech. Rock. Eng. 49 (6), 2437–2456. https://doi.org/10.1007/s00603-015-0731-0.